

Design and implementation of a novel architecture for physical human-UAV interaction

Sujit Rajappa¹, Heinrich Bülfhoff¹ and Paolo Stegagno^{1,2}

Abstract

Interaction between humans and unmanned aerial vehicles is a promising field for future applications. However, current interfacing paradigms either imply the presence of intermediary hardware as monitors, joysticks and haptic devices, or are limited to visual/auditory channels with hand gestures, voice recognition, or interpretation of face poses and body postures. Another paradigm, physical human–robot interaction, which is based on mutual exchange of forces, is popular when dealing with robotic arms and humanoids, while unmanned aerial vehicles are usually considered too dangerous and lack proper interaction surfaces to exchange forces. In this paper, we address the problem of physical human–unmanned aerial vehicle interaction and we propose a straightforward approach to allow a human to intuitively command an unmanned aerial vehicle through exchanges of forces. Using a residual based estimator, we estimate the external forces and torques acting on the unmanned aerial vehicle. Through the employment of a sensor ring, we are able to separate the human interaction forces from additional disturbances as wind and parameter uncertainties. This knowledge is used inside a control framework where the human is allowed to change the desired trajectory by simply applying forces on the unmanned aerial vehicle. The system is validated with multiple hardware-in-the-loop simulations and experiments in which we try different interaction modalities.

Keywords

Human–unmanned aerial vehicle interaction, aerial robot, unmanned aerial vehicle, admittance control, nonlinear observer, force estimator

1. Introduction

Unmanned aerial vehicles (UAVs) are gaining increasing attention among researchers and funding agencies. In particular, quadrotors are very popular for research purposes due to their ability to vertically takeoff and land, unsophisticated mechanical design and relatively simple system dynamics. With the advancements in computer vision and control techniques, quadrotors are now able to achieve versatile tasks, like autonomous navigation and (Fraundorfer et al., 2012; Heng et al., 2011), search and rescue (Mueggler et al., 2014), goods transportation (Palunko et al., 2012), construction (Augugliaro et al., 2014), aerial acrobatics (Lupashin et al., 2010; Mellinger et al., 2012; Ritz et al., 2012), grasping (Lindsey et al., 2011; Pounds et al., 2011) and aerial manipulation (Gioioso et al., 2014; Lippiello and Ruggiero, 2012; Orsag et al., 2013).

Most of the current applications involve flying in areas that are hardly accessible for humans. However, every year an increasing number of commercial platforms are hitting the market and becoming available to companies and the general public. Such a trend will eventually call for integration of quadrotors inside human-populated areas and

facilities. Some form of interaction between the UAVs and the humans will become necessary in order to exchange information and many foreseeable applications will also involve some form of physical contact and force exchange (i.e. physical interaction).

In assisting human workers, for example, a UAV may be required to deliver a tool directly to the hand of a user. Similar tasks have been performed with humanoid robots and manipulators using an active or passive compliance mechanism (e.g. through impedance control, variable stiffness actuators, or compliant joints and links) to account for uncertainties and provide a safe and pleasant interaction

¹ Autonomous Robotics and Human-Machine Systems group, Max Planck Institute for Biological Cybernetics, Germany

² Department of Ocean Engineering, University of Rhode Island, USA

Corresponding author:

Sujit Rajappa, Autonomous Robotics and Human-Machine Systems group, Max Planck Institute for Biological Cybernetics, Spemannstraße 38, 72076 Tübingen, Germany.

Email: sujit.rajappa@tuebingen.mpg.de; sujitraj369@gmail.com

experience (e.g. Edsinger and Kemp, 2007). In the experimental section of this article (Section 9), we will show how we can obtain similar compliant behaviors on UAVs.

Similarly, compliant behaviors have been proven to be effective in kinesthetic trajectory teaching to allow untrained users to set up robotic systems (e.g. Kronander and Billard, 2014). In this case, during the learning phase robots are expected to follow the lead of the operator without opposing resistance (i.e. by admitting the interaction forces applied by the operator). An attempt to replicate this behavior on UAVs have been presented by Sharma et al. (2013), in which a Laban-trained artist authored quadrotor motions by holding and puppeteering a quadrotor prop in a motion-capture tracked space. The authored motions were then replicated by the UAV in an experiment to evaluate the feasibility and impact of UAVs communicating through expressive motion paths. While the concept is indeed interesting, the method employed for the trajectory learning could lead to unfeasible trajectories for the UAV. For example, the artist could apply too much acceleration, or try to use the attitude of the UAV to express his feelings. Doing the same learning task with an actual quadrotor in flight would force the operator to choose feasible trajectories.

However, most works in human–robot interaction (HRI) involving UAVs are limited to recognizing voice commands, hand gestures, body and face poses, since aerial vehicles are still considered dangerous and not safe for physical human–robot interaction (PHRI). Among many reasons, the most important are:

- (a) the lack of an established hardware and software framework for physical human–UAV interaction (PHUI);
- (b) the lack of a proper interaction surface.

The goal of this work is to fill this gap by developing the technology to perform PHUI, implementing a setup that allows exchanges of forces between humans and UAVs and the methodologies to detect, interpret and react to such forces. Our setup includes a ring enclosing the propellers, with the twofold purpose of protecting an interacting human and providing an interaction surface equipped with appropriate sensors to detect the applied forces. Albeit safety is not explicitly considered in this work, both the presence of an interaction surface interposed between the user and the propellers, as well as the behavior chosen for the UAV in case of physical interaction (the motion in the opposite direction with respect to the interacting force) provide some degree of safety for the user. Further considerations on safety will be given in Section 10.

1.1. Related works

In the context of aerial robotics, HRI has been explored mostly by considering either intermediary physical interfaces such as monitors, joysticks and haptic devices, or visual and auditory sensory channels. Quigley et al. (2004) discussed different paradigms for human–UAV interfacing,



Fig. 1. Our quadrotor setup for PHUI.

with a detailed qualitative as well as quantitative performance analysis. The use of haptic interfaces for HRI with UAVs have been explored by Lee et al. (2013). Some authors studied how to replace the intermediary interfaces with an Red Green Blue-Depth (RGB-D) sensor connected to a ground control station. With this setup, Pfeil et al. (2013) explored the possibility of using the upper body to communicate with a UAV. Similarly, Sanna et al. (2013) implemented a command set by interpreting gestures and body postures detected through a Kinect sensor. Inevitably, the presence of an intermediary interface, be it a joystick or an RGB-D sensor, allows a less direct and intuitive approach to command the UAV, relying on coded command sets that need to be known a priori by the user. Moreover, the presence of a ground control station limits the portability of the system.

Many authors have studied more direct interaction paradigms by equipping cameras and RGB-D sensors directly on the UAV. Ng and Sharlin (2011) studied a gesture-based interaction scheme to communicate with the UAV based on a multimodal falconry metaphor. Lichtenstern et al. (2012) developed a command set for multi-robot systems using hand gestures recognized through an RGB-D sensor mounted on one of the UAVs. Nasser et al. (2013) used an active RGB-D sensor with vision based ego-motion cancellation to recognize and respond to hand gestures for high level tasks such as filming, landing, etc. Another approach by Monajjemi et al. (2013) uses a front facing camera for face tracking and gesture recognition to command robot teams. In the work by Nagi et al. (2014), a machine vision technique is used to control UAVs using face poses and hand gestures. Cauchard et al. (2015) conducted an evaluation study through Wizard-of-Oz elicitation about how users would naturally interact with drones, suggesting that it could be with voices, gestures or both. While these setups allow more intuitive first-person interaction, the necessity to process in real time the readings of highly informative sensors requires significant computational power. Moreover, despite the first person perspective,

many vision-based setups still require the knowledge of pre-coded commands. Conversely, with our setup:

- (a) PHUI can be performed through the readings of only a few button sensors, which can be easily processed onboard;
- (b) the reactive behavior of the UAV that we have implemented is intuitive and does not require any a priori knowledge.

Finally, instead of focusing on the command of the UAV, which accounts for an information flow from the human to the UAV, some authors have investigated novel methods to convey information from the UAV to the operator. Szafir et al. (2015) explored the visual communication of the directionality and intent of the aerial vehicle to the human user by means of coordinated lighting of a ring of light emitting diodes (LEDs). Cauchard et al. (2016) have studied how emotions can be encoded into the UAV path and speed. In order to allow bidirectional information flow, our setup could be complemented with these methodologies. For example, as we have developed a ring similar to the one proposed by Szafir et al. (2015), minimal additional hardware and payload would be required to create a bidirectional interaction surface.

Although rich, the above literature did not address PHUI. However, in recent years many works have been developed enabling technologies that can be employed for PHUI. Some works focus on new mechanical designs. For example, Briod et al. (2014) developed the gimbal, which allows stable UAV flight even in the event of collisions thanks to the outer protective frame. With respect to this work, we also try to address the PHUI by means of designing a suitable and versatile software architecture which can be particularized for different tasks. Other works focus on the problem of making and keeping contact with an object in the environment. Fumagalli et al. (2012) designed an attitude controller along with a passivity-based controller for contact inspection using aerial manipulation. This methodology has been further expanded by using an impedance-force control hybrid architecture by Scholten et al. (2013), and modified impedance control by Fumagalli and Carloni (2013). A force control approach with an external feedforward signal has been used by Albers et al. (2010).

When dealing with PHUI, it is important to estimate and characterize the external wrench (force and torque) acting on the UAV. Augugliaro and D'Andrea (2013), proposed an unscented Kalman filter in order to estimate the external wrench. To the best of our knowledge, this is also the only work which explicitly considers PHUI by proposing the use of an admittance controller. Bellens et al. (2012) investigated the problem of estimating the external wrench in the context of a hybrid pose/wrench control for a contact maintenance task. A force sensor was used as an estimator by Nguyen and Lee (2013). An alternative Lyapunov-based nonlinear observer for estimating the external wrench has

been proposed by Yüksel et al. (2014) and numerically validated. An external wrench estimation method based on the generalized momenta developed by Magrini et al. (2014) for an arm manipulator, has been employed in the estimation of the external wrench acting on an aerial vehicle (Ruggiero et al., 2014; Tomic and Haddadin, 2015). In particular, Tomic and Haddadin (2015) used this approach for collision detection, where they further separate the different contact forces from the aerodynamic disturbances based on the natural contact frequency characteristics. To the best of our knowledge, in the context of UAVs this is the only work which tries to characterize the external wrench by simultaneously considering disturbances and contact forces.

From the control perspective, with PHUI it is important to ensure stable flight and disturbance rejection through robust control techniques. Controllers in the literature include adaptive control methods (Antonelli et al., 2013; Palunko et al., 2012; Roberts and Tayebi, 2009), model predictive control approaches (Alexis et al., 2011; Raffo et al., 2010), backstepping, sliding mode (Bouabdallah and Siegwart, 2005, 2007) and super twisting controllers (Derafa et al., 2012; Rajappa et al., 2016).

1.2. Methodologies

The main objective of our work is to develop a framework and platform which allows PHUI. In order to achieve this objective, we employ the momenta-based external wrench observer developed by Tomic and Haddadin (2015) and Ruggiero et al. (2014). Using a custom-designed sensor ring, we proceed to characterize the external wrench by separating human interaction forces from external disturbances through the formulation of a quadratic optimization problem. We then implement an admittance control framework where we change the desired trajectory based on the interaction wrenches by manipulating the dynamical response of the aerial vehicle so that it behaves as a mass-spring-damper system. This control framework also includes a disturbance compensated geometric controller (Lee et al., 2010) for tracking the resulting trajectory. Therefore, in the context of PHUI the contribution of this work is:

- (a) a hardware design for PHUI, including a sensor ring which provides an interaction surface and useful data for the characterization of the external wrench;
- (b) a methodology for the separation of the forces/torques applied by an interacting human from generic disturbances;
- (c) the general architecture of the estimation and control framework which allows a human to provide an intuitive force command to the UAV while the disturbances are rejected by the controller.

In addition, we provide an extensive experimentation in which we show how varying only one parameter of the admittance control is enough to provide a wide range

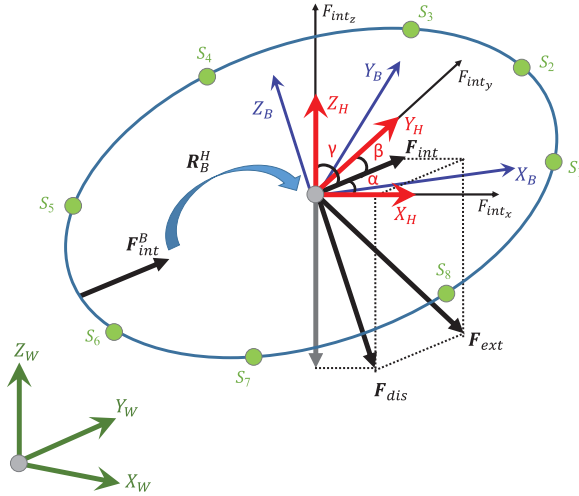


Fig. 2. Visualization of the main frames and quantities: the world frame \mathcal{F}_W in green; the body frame \mathcal{F}_B in blue; the horizontal frame \mathcal{F}_H in red; external \mathbf{F}_{ext} , disturbance \mathbf{F}_{dis} and interaction \mathbf{F}_{int} forces in black; green circles represent the sensors.

of behaviors suitable for several different applications. Although this is not novel in general (i.e. this concept has already been successfully applied on manipulator arms), to the best of our knowledge this is the first work to show this concept applied to UAVs. Clearly, adding the sensor ring to the UAV decreases its payload and flight time. However, most of the additional weight is due to the ring which replaces propeller guards, while the actual sensors account for only a few grams. Hence, with a smart design of the propeller guards we are able to turn them into an interactive surface at virtually no cost.

The rest of the sections are organized as follows. We introduce the dynamic model of the quadrotor and the problem formulation in Section 2. Our system architecture is described in Section 3. The hardware setup is discussed in Section 4. The external wrench estimator and the optimization problem to distinguish the disturbance and the interaction wrenches is detailed in Section 5. The control architecture is explained in Section 6. The proposed estimator and control algorithm is verified through physical hardware-in-loop simulations in Section 7. Real UAV experiments are performed in order to validate the external wrench observer (Section 8) and the whole system (Section 9). Section 10 concludes the paper.

2. Problem setting

The quadrotor UAV is modeled as a rigid body moving in 3D space. The world inertial frame in which the quadrotor flies is denoted as $\mathcal{F}_W : \{\mathbf{O}_W, \mathbf{X}_W, \mathbf{Y}_W, \mathbf{Z}_W\}$ and the body frame attached to the quadrotor is defined as $\mathcal{F}_B : \{\mathbf{O}_B, \mathbf{X}_B, \mathbf{Y}_B, \mathbf{Z}_B\}$, where \mathbf{O}_B coincides with the quadrotor Center of Mass (CoM). Let $\mathbf{p}_W = [x \ y \ z]^T \in \mathbb{R}^3$ describe the position of \mathbf{O}_B in \mathcal{F}_W and let $\boldsymbol{\Theta}_W = [\phi \ \theta \ \psi]^T \in$

\mathbb{R}^3 be the standard roll, pitch and yaw angles respectively, which describe the orientation of \mathcal{F}_B in \mathcal{F}_W , with $\phi, \theta \in [-\pi/2, \pi/2]$ and $\psi \in [0, 2\pi]$. Figure 2 presents a visualization of the reference frames and other important quantities.

The basic quadrotor states are therefore

$$\boldsymbol{\xi}_W = [\mathbf{p}_W^T \ \boldsymbol{\Theta}_W^T]^T = [x \ y \ z \ \phi \ \theta \ \psi]^T. \quad (1)$$

Let $\mathbf{R}_B^W = \mathbf{R}_z(\psi)\mathbf{R}_y(\theta)\mathbf{R}_x(\phi) \in \mathbb{R}^{3 \times 3}$ represent the rotation between \mathcal{F}_B and \mathcal{F}_W

$$\mathbf{R}_B^W = \begin{pmatrix} c_\psi c_\theta & c_\psi s_\theta s_\phi - s_\psi c_\phi & c_\psi s_\theta c_\phi + s_\psi s_\phi \\ s_\psi c_\theta & s_\psi s_\theta s_\phi + c_\psi c_\phi & s_\psi s_\theta c_\phi - c_\psi s_\phi \\ -s_\theta & c_\theta s_\phi & c_\theta c_\phi \end{pmatrix}, \quad (2)$$

where $c_\star = \cos(\star)$, $s_\star = \sin(\star)$ and \mathbf{R}_z , \mathbf{R}_y , \mathbf{R}_x denote the 3×3 fundamental rotation matrices around the Z , Y and X axes respectively. We define also the horizontal frame \mathcal{F}_H : $\{\mathbf{O}_H, \mathbf{X}_H, \mathbf{Y}_H, \mathbf{Z}_H\}$ such that $\mathbf{O}_H \equiv \mathbf{O}_B$, $\mathbf{Z}_H \parallel \mathbf{Z}_W$ and $\psi_H = 0$, where ψ_H is the yaw angle of the UAV expressed in \mathcal{F}_H . Then, the rotation matrix between \mathcal{F}_W and \mathcal{F}_H is $\mathbf{R}_H^W = \mathbf{R}_z(\psi)$ and the rotation matrix between \mathcal{F}_H and \mathcal{F}_B is $\mathbf{R}_B^H = \mathbf{R}_y(\theta)\mathbf{R}_x(\phi)$. Hence the state of the UAV in \mathcal{F}_H is

$$\boldsymbol{\xi}_H = [\mathbf{p}_H^T \ \boldsymbol{\Theta}_H^T]^T = [0 \ 0 \ 0 \ \phi \ \theta \ 0]^T. \quad (3)$$

The actuation system of the quadrotor consists in four motor-propeller pairs attached to four rigid arms. This configuration allows us to command independently three torques $\boldsymbol{\tau} = [\tau_x \ \tau_y \ \tau_z]^T \in \mathbb{R}^3$ around the three axes \mathbf{X}_B , \mathbf{Y}_B , \mathbf{Z}_B and one force $\rho \in \mathbb{R}_0^+$ called thrust along \mathbf{Z}_B . From the control point of view, recent research proved convenient (Lee et al., 2010) to define the translational dynamics of quadrotors in terms of the world frame \mathcal{F}_W and the rotational dynamics in terms of the quadrotor body frame \mathcal{F}_B . Therefore, we express the generalized velocity vector states as

$$\boldsymbol{\xi} = [\dot{\mathbf{p}}_H^T \ \boldsymbol{\omega}_B^T]^T, \quad (4)$$

where $\dot{\mathbf{p}}_H \in \mathbb{R}^3$ is the linear velocity of the quadrotor in \mathcal{F}_W expressed in \mathcal{F}_H , and $\boldsymbol{\omega}_B = [p \ q \ r]^T \in \mathbb{R}^3$ is the angular velocity of the quadrotor in \mathcal{F}_W expressed in the \mathcal{F}_B .

Since it will be convenient in the following formulation, we express the translational dynamics of the quadrotor in \mathcal{F}_W , while we express the rotational dynamics in \mathcal{F}_B . Using the standard Newton–Euler equations of motion, the dynamical model of the quadrotor can be written as (Lee et al., 2013)¹

$$m\ddot{\mathbf{p}}_W = -mge_3 + \rho\mathbf{R}_B^W e_3 + \mathbf{R}_H^W \mathbf{F}_{\text{ext}} \quad (5)$$

$$\mathbf{I}_B \dot{\boldsymbol{\omega}}_B = -\boldsymbol{\omega}_B \times \mathbf{I}_B \boldsymbol{\omega}_B + \boldsymbol{\tau} + \boldsymbol{\tau}_{\text{ext}} \quad (6)$$

$$\dot{\boldsymbol{\Theta}}_W = \mathbf{T}(\boldsymbol{\Theta}_W) \boldsymbol{\omega}_B \quad (7)$$

where m is the mass of the quadrotor, $e_3 = [0 \ 0 \ 1]^T$ is the unitary vector along the Z -axis, g is the gravity accele-

ration, $\ddot{\mathbf{p}}_W \in \mathbb{R}^3$ is the acceleration of the quadrotor in \mathcal{F}_W , $\dot{\boldsymbol{\omega}}_B = [\dot{p} \ \dot{q} \ \dot{r}]^T \in \mathbb{R}^3$ is the angular acceleration of the quadrotor with respect to \mathcal{F}_B

$$\mathbf{I}_B = \begin{bmatrix} I_{xx} & 0 & 0 \\ 0 & I_{yy} & 0 \\ 0 & 0 & I_{zz} \end{bmatrix} \quad (8)$$

is the diagonal inertia matrix of the quadrotor in body frame, $\mathbf{T}(\Theta_W) \in \mathbb{R}^{3 \times 3}$ is the transformation matrix from $\boldsymbol{\omega}_B$ to the Euler angle rates $\dot{\Theta}_W \in \mathbb{R}^3$ and $\mathbf{F}_{\text{ext}} = [F_{\text{ext}x} \ F_{\text{ext}y} \ F_{\text{ext}z}]^T \in \mathbb{R}^3$, $\boldsymbol{\tau}_{\text{ext}} = [\tau_{\text{ext}x} \ \tau_{\text{ext}y} \ \tau_{\text{ext}z}]^T \in \mathbb{R}^3$ represent all additional forces in \mathcal{F}_H and torques in \mathcal{F}_B respectively acting on the quadrotor due to disturbances and external forces. Note that the gravity acceleration $g e_3$ does not need to be rotated from \mathcal{F}_W to \mathcal{F}_H , since its only non-zero component is not affected by this rotation being $\mathbf{Z}_H \parallel \mathbf{Z}_W$. Note that it is also possible to express equation (5) in \mathcal{F}_H as

$$m\ddot{\mathbf{p}}_H = -mge_3 + \rho \mathbf{R}_B^H e_3 + \mathbf{F}_{\text{ext}}. \quad (9)$$

While for control purpose we will use the system defined by equations (5) to (7), in the estimator design it will be convenient to consider the system defined by equations (9), (6) and (7).

2.1. Model of the external wrench

We define the external wrench $\Lambda_{\text{ext}} = [\mathbf{F}_{\text{ext}}^T \ \boldsymbol{\tau}_{\text{ext}}^T]^T \in \mathbb{R}^6$ as the stacked vector of the external forces in \mathcal{F}_H and torques in \mathcal{F}_B applied in the CoM O_B . It represents the resultant of all forces and torques acting on the UAV which are not due to the nominal actuation or the nominal gravity force acting on the quadrotor.

Given this very generic definition, it is clear that Λ_{ext} may include a large variety of terms. However, we can separate these terms into two main categories. In the first category, we consider all disturbances due to either external causes, such as wind, or to mismatches between the nominal and real parameters of the model, for example a difference between the nominal and real mass of the UAV. The resultant of all these forces and torques is modeled as one disturbance wrench $\Lambda_{\text{dis}}^B = [\mathbf{F}_{\text{dis}}^B]^T \ \boldsymbol{\tau}_{\text{dis}}^T]^T \in \mathbb{R}^6$ expressed in \mathcal{F}_B applied in the CoM of the UAV. The disturbance force $\mathbf{F}_{\text{dis}}^B$ can also be expressed in the horizontal frame \mathcal{F}_H by the use of an appropriate rotation matrix

$$\Lambda_{\text{dis}} = \mathbf{J}_{H_{\text{dis}}} \Lambda_{\text{dis}}^B = \begin{bmatrix} \mathbf{R}_B^H & \mathbf{0}_3 \\ \mathbf{0}_3 & \mathbf{I}_3 \end{bmatrix} \Lambda_{\text{dis}}^B. \quad (10)$$

The forces and torques resulting from physical interaction with humans lie in the second category. In general, one or more interacting humans apply q independent wrenches $\Lambda_{\text{int}_i}^B = [\mathbf{F}_{\text{int}_i}^B]^T \ \boldsymbol{\tau}_{\text{int}_i}^T]^T \in \mathbb{R}^6$, $i = 1, \dots, q$, where $\mathbf{F}_{\text{int}_i}^B$ and $\boldsymbol{\tau}_{\text{int}_i}$ are both expressed in \mathcal{F}_B . The application points \mathbf{p}_i , $i = 1, \dots, q$ expressed in \mathcal{F}_B are in general all different from each other. In order to introduce these wrenches in equations (5) and (6), we first need to express the forces in \mathcal{F}_H as

$\mathbf{F}_{\text{int}_i}^H = \mathbf{R}_B^H \mathbf{F}_{\text{int}_i}^B$. Then we need to compute their effect on the CoM, since they cause additional torques $-[\mathbf{R}_B^H \mathbf{p}_i] \wedge$ where $[\cdot] \wedge$ is the map from \mathbb{R}^3 to the skew-symmetric matrix

$$\left[\begin{bmatrix} x \\ y \\ z \end{bmatrix} \right] \wedge = \begin{bmatrix} 0 & -z & y \\ z & 0 & -x \\ -y & x & 0 \end{bmatrix}. \quad (11)$$

Hence, the generic wrench $\Lambda_{\text{int}_i}^B$ acts on the system as

$$\Lambda_{\text{int}_i} = \mathbf{J}_{H_i} \Lambda_{\text{int}_i}^B = \begin{bmatrix} \mathbf{I}_3 & -[\mathbf{R}_B^H \mathbf{p}_i] \wedge \\ \mathbf{0}_3 & \mathbf{I}_3 \end{bmatrix} \begin{bmatrix} \mathbf{R}_B^H & \mathbf{0}_3 \\ \mathbf{0}_3 & \mathbf{I}_3 \end{bmatrix}^T \Lambda_{\text{int}_i}^B, \quad (12)$$

where $\mathbf{0}_3$ and \mathbf{I}_3 are respectively the 3×3 null and identity matrices.

Denoting with $\Lambda_{\text{int}} = [\mathbf{F}_{\text{int}}^T \ \boldsymbol{\tau}_{\text{int}}^T]^T \in \mathbb{R}^6$ the resultant of the interaction wrenches, then the total external wrench is

$$\Lambda_{\text{ext}} = \Lambda_{\text{dis}} + \Lambda_{\text{int}} = \mathbf{J}_{H_{\text{dis}}} \Lambda_{\text{dis}}^B + \sum_{i=1}^q \mathbf{J}_{H_i} \Lambda_{\text{int}_i}^B. \quad (13)$$

2.2. Force/torque detectors

The UAV is equipped with n sensing devices s_1, \dots, s_n attached to n points \mathbf{p}_{s_i} , $i = 1, \dots, n$ (in \mathcal{F}_B) that are able to measure a force and/or torque applied in their particular location. In the following, we will refer to the \mathbf{p}_{s_i} 's as points of contact (PoC). The measured forces/torques are provided as m -bit quantized signals, with a quantization interval for s_i of \mathbf{F}_{sa_i} for the forces (if measured) and $\boldsymbol{\tau}_{sa_i}$ for the torques (if measured).

This generic formulation includes different types of sensor devices, from proper force/torque sensors to simple push buttons. In our hardware setup we will use the latter, hence we proceed here to particularize their case. However, most of the findings in this work are compatible with more complex sensing devices.

Push buttons can be modeled as simple 1-bit quantization force sensors measuring a force acting along the normal vector to the button surface. Let s_i be a push button sensor, and let

$$\mathbf{n}_i = [\cos(\alpha_i) \ \cos(\beta_i) \ \cos(\gamma_i)]^T \quad (14)$$

be the incoming normal vector to its surface in \mathcal{F}_B , specified through its direction cosines. In the previous expression, α_i , β_i , γ_i are the angles between \mathbf{n}_i and the axes \mathbf{X}_B , \mathbf{Y}_B , \mathbf{Z}_B respectively.

Then, the sensor can provide two possible measurements:

- (a) 0, which means that there is no detected force applied in \mathbf{p}_{s_i} , hence s_i is inactive;
- (b) 1, which means that there is a force $\mathbf{F}_{\text{int}_i}^B = \|\mathbf{F}_{\text{int}_i}^B\| \mathbf{n}_i$ applied in \mathbf{p}_{s_i} , with $\|\mathbf{F}_{\text{int}_i}^B\| > \mathbf{F}_{sa_i}$, and in this case s_i is active.

In the rest of the paper, we assume that at a given time instant only $N \leq n$ out of $\{s_1, \dots, s_n\}$ are active. Without loss of generality we rename the active sensors, their PoCs,

their quantization interval and the normal vector to their surface respectively S_i , \mathbf{P}_{S_i} , $\mathbf{F}_{S_{Ai}}$ and \mathbf{N}_i , for $i = 1, \dots, N$. We will also denote with $\Lambda_{\text{int}_i}^B = [\mathbf{F}_{\text{int}_i}^{BT} \ 0 \ 0 \ 0]^T$ the interaction wrench acting on \mathbf{P}_{S_i} .

3. System architecture

The main goal of this work is to develop an estimation and control framework such that physical interactions of humans with the UAV results in actions from the quadrotor that second the interaction forces.

Our system architecture (see Figure 3) is composed of two main block chains. The first estimation chain is in charge of estimating the relevant dynamic quantities that are needed in the second control chain. In particular, the system will compute estimates $\hat{\Lambda}_{\text{int}_i}^B, i = 1, \dots, N$, $\hat{\Lambda}_{\text{dis}}^B$ of the interaction and disturbance wrenches respectively, based on the knowledge of ρ , τ , ξ_H , ζ , S_i , \mathbf{P}_{S_i} , $\mathbf{F}_{S_{Ai}}$ and \mathbf{N}_i , for $i = 1, \dots, N$.

The estimation chain consists of a two step system. In the first step, the system state $\dot{\mathbf{p}}_H$, as well as the control commands ρ , τ are used to compute a minimal error estimate $\hat{\Lambda}_{\text{ext}}$ of the total external wrench Λ_{ext} acting on the quadrotor, using a momenta based residual estimator.

This estimate is then decomposed into estimates of the interaction $\hat{\Lambda}_{\text{int}_i}^B, i = 1, \dots, N$ and disturbance wrenches $\hat{\Lambda}_{\text{dis}}^B$ according to equation (13), in which interaction forces are considered to be applied on the active sensors S_1, \dots, S_N . In this step, the sensor readings, as well as the sensor parameters are used in a quadratic programming problem which tries to explain the estimated $\hat{\Lambda}_{\text{ext}}$ using the minimum norm stacked vector $[\hat{\Lambda}_{\text{dis}}^{BT} \ \hat{\Lambda}_{\text{int}_1}^{BT} \ \dots \ \hat{\Lambda}_{\text{int}_N}^{BT}]^T$.

The control chain is designed to perform a trajectory tracking. In the beginning, the desired trajectory \mathbf{p}_d , $\dot{\mathbf{p}}_d$, $\ddot{\mathbf{p}}_d$ is produced by a trajectory generator. However, when the interaction wrench estimates are non-zero, an admittance controller modifies it based on their resultant $\hat{\Lambda}_{\text{int}}$. The new reference trajectory is passed to a geometric trajectory tracking controller which uses the knowledge of the estimated disturbance wrench $\hat{\Lambda}_{\text{dis}}$ to reject it through a feedforward term.

4. Hardware-software design

The UAV platform employed in this work is a MK-Quadro quadrotor from MikroKopter.² The MK-Quadro consists of four propeller arms, each one equipped with a motor controller, a brushless motor and a 10" propeller. The MK-Quadro has an onboard 8-bit microcontroller, which is used to perform the low-level control, transferring the control commands from the high-level controller to the motor controller. The microcontroller board includes an inertial measurement unit (IMU) composed of two three-axis analog sensors: an accelerometer with measurement range of $\pm 2g$ and a gyroscope with measurement range $\pm 300^\circ/\text{s}$, both

read with a 10-bit analog to digital converter. The board communicates with the brushless motor controllers through a standard I²C bus.

The standard MikroKopter firmware has been replaced with our own software that allows us to control the robot through a serial XBee channel operating at 115,200 Bd baud rate. The command sent to the microcontroller at ~ 120 Hz, consists of the setpoints for the brushless motors, which are computed on an offboard desktop PC. The platform is powered by a 2600 mAh LiPo battery that provides approximately 10 min of flight. Additionally, the quadrotor is equipped with Odroid-XU3, a double quad core ARM microprocessor board. The power to the Odroid and its components are provided by a 5 V step-down voltage regulator connected to the LiPo battery. The Odroid is also fitted with Wi-Fi adapter, which is useful for exchanging data with the ground station.

The UAV shown in Figure 1, is retrofitted with four additional arms. Extenders at the end of each arm are fixed so that the whole propeller is always inside the diameter of the UAV setup. One 12 mm square momentary button is mounted at the end of each extender. A floating ring structure encloses the whole quadrotor while being always in contact with the buttons as shown in Figure 4. In this configuration, the buttons are all coplanar and lie on the same XY plane of the CoM. Moreover, they are equally spaced along the inner circumference of the ring with an angular distance of 45° . In this way, a force applied to any point of the ring in the direction of the CoM of the quadrotor activates one or more buttons depending on the location of the point of contact. For example, if the PoC is near one button, that button will be activated, whereas a PoC between two buttons, will cause the activation of both. Naming the sensors as s_1, \dots, s_8 (as shown in Figure 2), the interaction points and the normal vectors are in the form

$$\mathbf{p}_{s_i} = \mathbf{R}_z \left(\frac{\pi(i-1)}{4} \right) L e_1, \quad \mathbf{n}_i = -\mathbf{R}_z \left(\frac{\pi(i-1)}{4} \right) e_1,$$

where $L = 0.34$ m is the length of the arms and $e_1 = [1 \ 0 \ 0]^T$. The buttons are connected to the general-purpose input/output (GPIO) ports of the Odroid-XU3 board which communicates them to the base station through a robot operating system (ROS) topic over Wi-Fi connection.

The main control and estimation algorithms are performed in the base station, which is a ROS enabled Ubuntu 14.04 PC. The state of the UAV in the 10×10 m flying arena is provided at 120 Hz by a motion capture system (VICON), which is also used to collect ground truth data.

5. Estimation of the external, interactive and disturbance wrenches

Our goal is to estimate the interaction $\Lambda_{\text{int}_i}^B, i = 1, \dots, N$ and disturbance Λ_{dis}^B wrenches acting on the UAV. In order to achieve this, we follow a two-step procedure. First, we employ a residual based estimator to estimate the total

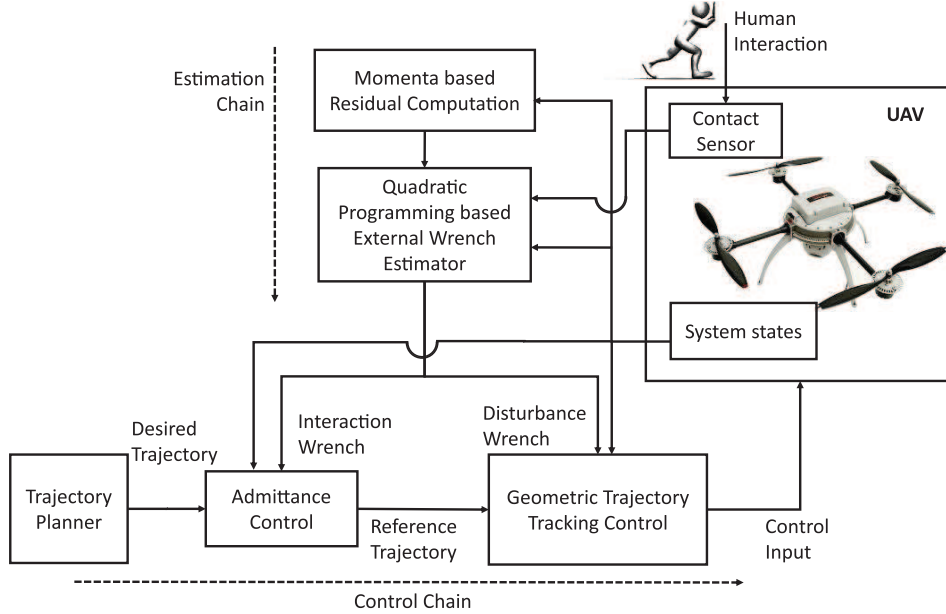


Fig. 3. Block scheme of the system architecture for human-UAV interaction.

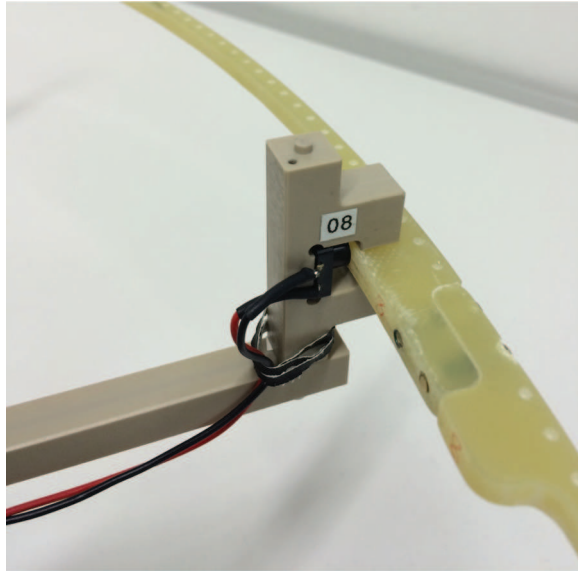


Fig. 4. Close-up view of one of the arm extenders with the button and the interaction ring.

external wrench Λ_{ext} . Then, we decompose this wrench into multiple components $\Lambda_{\text{int}_i}^B, i = 1, \dots, N$, Λ_{dis}^B based on a least square principle.

5.1. Estimation of the external wrench

In order to estimate the external wrench Λ_{ext} acting on the quadrotor, we have implemented a residual based estimator which follows the formulation proposed in literature for robotic arms (De Luca and Mattone, 2003; Takakura et al., 1989). Recently (Ruggiero et al., 2014; Tomic and Hadadin, 2015), this approach has been extended also for UAV

applications. The estimator used in this work follows a similar approach. For the sake of completeness, we summarize its working principle.

For its mathematical description, it is convenient to express the dynamical model of the quadrotor given by equations (9) and (6) following the Lagrangian formulation

$$\mathbf{M}\dot{\boldsymbol{\zeta}} + \mathbf{C}(\boldsymbol{\zeta})\boldsymbol{\zeta} + \mathbf{G} = \boldsymbol{\Lambda} + \boldsymbol{\Lambda}_{\text{ext}}, \quad (15)$$

where

$$\mathbf{M} = \begin{bmatrix} m\mathbf{I}_3 & \mathbf{0}_3 \\ \mathbf{0}_3 & \mathbf{I}_B \end{bmatrix} \in \mathbb{R}^{6 \times 6} \quad (16)$$

is the diagonal, positive definite inertial matrix. The matrix

$$\mathbf{C}(\boldsymbol{\zeta}) = \begin{bmatrix} \mathbf{0}_3 & \mathbf{0}_3 \\ \mathbf{0}_3 & \begin{bmatrix} 0 & I_{zz}r & -I_{yy}q \\ -I_{zz}r & 0 & I_{xx}p \\ I_{yy}q & -I_{xx}p & 0 \end{bmatrix} \end{bmatrix} \in \mathbb{R}^{6 \times 6} \quad (17)$$

expresses the Coriolis and centrifugal terms, while \mathbf{G} is the gravitational vector given by

$$\mathbf{G} = [0 \ 0 \ mg \ 0 \ 0 \ 0]^T \in \mathbb{R}^6 \quad (18)$$

and $\boldsymbol{\Lambda} = [(\rho \mathbf{R}_B^H e_3)^T \ \boldsymbol{\tau}^T]^T \in \mathbb{R}^6$ is the nominal wrench due to the control input.

The external wrench estimator is based on the idea of the generalized momenta $\mathbf{Q} = \mathbf{M}\boldsymbol{\zeta}$, for which it is possible to write the following first-order dynamic equation

$$\dot{\mathbf{Q}} = \boldsymbol{\Lambda} + \boldsymbol{\Lambda}_{\text{ext}} + \mathbf{C}^T(\boldsymbol{\zeta})\boldsymbol{\zeta} - \mathbf{G}, \quad (19)$$

which is obtained from equation (15). Let the residual vector $r \in \mathbb{R}^6$ for the disturbance estimation of the quadrotor be defined as

$$r(t) = \mathbf{K}_I \left(\mathbf{Q} - \int_0^t (\boldsymbol{\Lambda} + \mathbf{C}^T(\boldsymbol{\zeta})\boldsymbol{\zeta} - \mathbf{G} + r) ds \right), \quad (20)$$

where $\mathbf{K}_I > 0$ is a diagonal positive-definite gain matrix. For $r(0) = 0$, the dynamic evolution of r satisfies

$$\dot{r} = \mathbf{K}_I (\mathbf{\Lambda}_{\text{ext}} - r), \quad (21)$$

which is an exponentially stable linear system driven by the external disturbance wrench. For the implementation of equation (20) at every time instant only the measure of the current ζ (i.e. velocity) and the knowledge of the commanded wrench $\mathbf{\Lambda}$ are required.

Equation (21) shows that the dynamic evolution of ' r ' has a stable first-order filter structure. Therefore, the transfer function of each component of the residual vector takes the form

$$\frac{r_I(s)}{\mathbf{\Lambda}_{\text{ext},I}(s)} = \frac{\mathbf{K}_I}{s + \mathbf{K}_I}, \quad I = 1, \dots, 6 \quad (22)$$

which has a unitary gain. Therefore, for "sufficiently" large gains, the evolution of $r_I(t)$ resembles $\mathbf{\Lambda}_{\text{ext},I}(t)$ and the dynamic residual in equation (21) becomes

$$r \simeq \mathbf{\Lambda}_{\text{ext}}. \quad (23)$$

Hence, we can use as estimator of the external wrench

$$\hat{\mathbf{\Lambda}}_{\text{ext}} = r, \quad (24)$$

where in general the symbol $\hat{\circ}$ indicates the estimated value of a quantity \circ .

Remark 1. *The evolution of the system defined by equation (21) is dictated by the gain matrix \mathbf{K}_I . In particular, the larger the value of the gains, the faster and more accurately the residual in equation (20) will converge to the actual value. On the other hand, too large values of \mathbf{K}_I will result in noisy (less precise) estimates. Hence, the gain matrix \mathbf{K}_I must be tuned taking into account these aspects. In this work we have used a gain of $\mathbf{K}_I = h\mathbf{I}_6$, where \mathbf{I}_6 is the 6×6 identity matrix, with $h = 5$ both in simulations (Section 7) and experiments (Section 9).*

5.2. Estimation of the disturbance and interaction wrenches

Clearly, the estimate of the external wrench from equation (24) accounts for both the interaction and disturbance wrenches. The interaction wrench further consists of the wrenches arising from different PoC, as specified in equation (13). In order to allow a safe PHUI, we need to compute separate estimates for all of these components.

In this work, we have considered that the wrenches arising from the human interaction are observed at one or more of the preselected points \mathbf{p}_{s_i} , where the sensors are installed. This assumption substantially reduces the number of constraints in the quadratic programming based optimization giving it a computational edge over considering a sensor surface (e.g. tactile sensor setup). However, provided that the sensors are deployed so that they can correctly describe any possible interaction wrench, this advantage comes at

no price, since the admittance controller will use the resultant of the wrenches estimated at the sensors' location (see Section 6.1) and not their specific values. Conversely, if the sensors are not located correctly a fraction or the whole interaction force may be interpreted as disturbance.

In our setup, we have deployed eight coplanar sensors pointing towards the CoM of the UAV which are able to describe any possible interaction force on the horizontal plane. In case an interaction force along the vertical axis or an interaction torque are applied, these components will be ignored and detected as disturbance. Similarly, if all the sensors were deployed pointing along the X -axis (e.g. only two sensors in the front and the back of the UAV), then the system would not be able to estimate interaction forces along the Y -axis.

By stacking the transposed matrices $\mathbf{J}_{H_{\text{dis}}}$, \mathbf{J}_{H_i} and the disturbance and interaction wrenches $\mathbf{\Lambda}_{\text{dis}}^B$, $\mathbf{\Lambda}_{\text{int}_i}^B$, the external wrench $\mathbf{\Lambda}_{\text{ext}}$ from equation (13) can be written as

$$\mathbf{\Lambda}_{\text{ext}} = [\mathbf{J}_{H_{\text{dis}}} \quad \mathbf{J}_{H_1} \quad \cdots \quad \mathbf{J}_{H_N}] \begin{bmatrix} \mathbf{\Lambda}_{\text{dis}}^B \\ \mathbf{\Lambda}_{\text{int}_1}^B \\ \vdots \\ \mathbf{\Lambda}_{\text{int}_N}^B \end{bmatrix}. \quad (25)$$

In the above expression, all $\mathbf{\Lambda}_{\text{int}_i}^B$ are applied in their real point of contact, whereas $\mathbf{\Lambda}_{\text{dis}}^B$ is acting in the CoM of the quadrotor. $\hat{\mathbf{\Lambda}}_{\text{dis}}^B$, $\hat{\mathbf{\Lambda}}_{\text{int}_i}^B$ being the estimates of $\mathbf{\Lambda}_{\text{dis}}^B$, $\mathbf{\Lambda}_{\text{int}_i}^B$, they can be related to the residual vector from equation (24)

$$r = \hat{\mathbf{\Lambda}}_{\text{ext}} = \underbrace{[\mathbf{J}_{H_{\text{dis}}} \quad \mathbf{J}_{H_1} \quad \cdots \quad \mathbf{J}_{H_N}]}_{\triangleq \mathbf{A}_1} \begin{bmatrix} \hat{\mathbf{\Lambda}}_{\text{dis}}^B \\ \hat{\mathbf{\Lambda}}_{\text{int}_1}^B \\ \vdots \\ \hat{\mathbf{\Lambda}}_{\text{int}_N}^B \end{bmatrix}, \quad (26)$$

where the matrix $\mathbf{A}_1 \in \mathbb{R}^{6 \times 6(N+1)}$ has always $\text{rank}(\mathbf{A}_1) = 6$.

In general, for $N > 0$ (hence, when at least one interaction force is present) the problem of finding $\hat{\mathbf{\Lambda}}_c^B$ from $\hat{\mathbf{\Lambda}}_{\text{ext}}$ by inverting equation (26) always admits infinite solutions. Therefore, we formulate the estimation of $\hat{\mathbf{\Lambda}}_c^B$ as the solution of a quadratic optimization problem in the form

$$\hat{\mathbf{\Lambda}}_c^B = \underset{\lambda \in \mathbb{R}^p}{\text{argmin}} \lambda^T \mathbf{D} \lambda + 2\mathbf{C}^T \lambda \quad (27)$$

$$\text{s. t. } \mathbf{A}\lambda \leq \mathbf{b} \quad (28)$$

where $p = 6(N+1)$, $\mathbf{D} \in \mathbb{R}^{p \times p}$ and $\mathbf{C} \in \mathbb{R}^{p \times 6}$ are appropriate weight matrices and $\mathbf{A} \in \mathbb{R}^{p \times q}$ and $\mathbf{b} \in \mathbb{R}^q$ defines q appropriate constraints.

Objective function. In the choice of \mathbf{D} and \mathbf{C} , we want to follow two main principles. First, since infinite solutions are possible, we want to have the minimal wrench configuration that explains the readings of the sensors and the

estimated external wrench. Therefore we choose $\mathbf{C} = \mathbf{0}_{p \times 6}$ and we select \mathbf{D} as a positive definite diagonal matrix whose eigenvalues are strictly positive. This choice ensures that there is a unique global minimum while the quadratic problem is solved. Secondly, the disturbance wrench $\hat{\Lambda}_\text{dis}^B$ should contain only the components of $\hat{\Lambda}_\text{ext}$ that cannot be explained through interaction wrenches according to the sensor readings. By choosing a matrix in the form

$$\mathbf{D} = \begin{pmatrix} w\mathbf{I}_6 & \mathbf{0}_6 & \cdots & \mathbf{0}_6 \\ \mathbf{0}_6 & \mathbf{I}_6 & \cdots & \mathbf{0}_6 \\ \vdots & \vdots & \ddots & \vdots \\ \mathbf{0}_6 & \mathbf{0}_6 & \cdots & \mathbf{I}_6 \end{pmatrix}, \quad (29)$$

with $w \gg 1$ we penalize $\hat{\Lambda}_\text{dis}^B$ in favor of the estimated interaction wrenches. Hence, we have selected $w = 50$ through a trial-and-error procedure. One limitation of this approach arises when both the disturbance and the interaction wrenches are in the same direction, since the disturbance can be explained by the sensor readings and will be accounted as an additional interaction wrench. In order to mitigate such an issue, it is possible to study an adaptive law which varies w over time.

In the following, we consider four constraints. While the first and the fourth are valid in general, the other two are specific for the type of sensor that we have used. Other constraints can be considered if the UAV is equipped with other types of sensors.

Constraint 1. $\hat{\Lambda}_c^B$ must respect $A_1 \hat{\Lambda}_c^B = \hat{\Lambda}_\text{ext} = r$.

This constraint is the direct application of equation (26).

Constraint 2. The interaction force $\hat{\mathbf{F}}_{\text{int}_i}^B$ lies along the normal vector \mathbf{N}_i .

The equation for this constraint can be found by taking into account the direction cosines of \mathbf{N}_i from equation (14). The relation between the direction cosines and the interaction forces for sensor S_i is

$$|\hat{\mathbf{F}}_{\text{int}_i}^B| = \frac{\hat{\mathbf{F}}_{\text{int}_{x_i}}^B}{\cos(\alpha_i)} = \frac{\hat{\mathbf{F}}_{\text{int}_{y_i}}^B}{\cos(\beta_i)} = \frac{\hat{\mathbf{F}}_{\text{int}_{z_i}}^B}{\cos(\gamma_i)}. \quad (30)$$

The following three constraints are equivalent to equation (30)

$$\begin{aligned} \hat{\mathbf{F}}_{\text{int}_{x_i}}^B \cos(\beta_i) - \hat{\mathbf{F}}_{\text{int}_{y_i}}^B \cos(\alpha_i) &= 0 \\ \hat{\mathbf{F}}_{\text{int}_{x_i}}^B \cos(\gamma_i) - \hat{\mathbf{F}}_{\text{int}_{z_i}}^B \cos(\alpha_i) &= 0 \\ \hat{\mathbf{F}}_{\text{int}_{y_i}}^B \cos(\gamma_i) - \hat{\mathbf{F}}_{\text{int}_{z_i}}^B \cos(\beta_i) &= 0 \end{aligned} \quad (31)$$

which in matrix form becomes

$$\underbrace{\begin{bmatrix} \cos(\beta_i) & -\cos(\alpha_i) & 0 \\ \cos(\gamma_i) & 0 & -\cos(\alpha_i) \\ 0 & \cos(\gamma_i) & -\cos(\beta_i) \end{bmatrix}}_{\triangleq A_2} \underbrace{\begin{bmatrix} \hat{\mathbf{F}}_{\text{int}_{x_i}}^B \\ \hat{\mathbf{F}}_{\text{int}_{y_i}}^B \\ \hat{\mathbf{F}}_{\text{int}_{z_i}}^B \end{bmatrix}}_{\triangleq b_2} = \begin{bmatrix} 0 \\ 0 \\ 0 \end{bmatrix}. \quad (32)$$

Note that the constraints in equation (32) exists for each active sensor S_1, \dots, S_N .

Constraint 3. Each sensor has a minimum activation force $F_{S_{a_i}} \in \mathbb{R}$.

Let $F_{S_{a_i}}$ be the minimum force required by the i -th sensor to be activated. Then

$$|\hat{\mathbf{F}}_{\text{int}_i}^B| \geq F_{S_{a_i}}. \quad (33)$$

By using the expression of the direction cosines to describe the force applied to each S_i , we obtain three more constraints for each sensor, which in matrix form are

$$\begin{bmatrix} \hat{\mathbf{F}}_{\text{int}_{x_i}}^B \\ \hat{\mathbf{F}}_{\text{int}_{y_i}}^B \\ \hat{\mathbf{F}}_{\text{int}_{z_i}}^B \end{bmatrix} \geq \underbrace{\begin{bmatrix} F_{S_{a_i}} \cos(\alpha_i) \\ F_{S_{a_i}} \cos(\beta_i) \\ F_{S_{a_i}} \cos(\gamma_i) \end{bmatrix}}_{\triangleq b_3}. \quad (34)$$

Constraint 4. The interaction torques $\tau_{\text{int}_{x_i}}, \tau_{\text{int}_{y_i}}$ are always zero.

This constraint is necessary because the torques around X_B and Y_B directly affect the rotational dynamics of the quadrotor given by equation (6). Since the quadrotor is an underactuated system, the roll and pitch angles cannot be selected independently.

However, if the UAV is fully actuated (Rajappa et al., 2015) this constraint can be reformulated to allow admittance of the interaction torques around X_B and Y_B . In matrix form, this constraint is

$$\begin{bmatrix} \hat{\tau}_{\text{int}_{x_i}} \\ \hat{\tau}_{\text{int}_{y_i}} \end{bmatrix} = \begin{bmatrix} 0 \\ 0 \end{bmatrix}. \quad (35)$$

Remark 2. The interaction torque $\hat{\tau}_{\text{int}_{z_i}}$ is not constrained to be identically null and it is estimated alongside $\hat{\mathbf{F}}_{\text{int}_i}^B$ because yaw can be set independently and does not get affected by the underactuation problem.

Optimization problem. The final form of the quadratic optimization problem is

$$\hat{\Lambda}_c^B = \underset{\lambda \in \mathbb{R}^p}{\operatorname{argmin}} \lambda^T \mathbf{D} \lambda \quad (36)$$

$$\text{s. t. } \begin{cases} A_1 \lambda = r \\ A_2 \lambda_i = b_{2i}, \quad i = 1, \dots, N \\ \lambda_i \geq b_{3i}, \quad i = 1, \dots, N \\ \lambda_{\tau_i} = 0, \quad i = 1, \dots, N \end{cases} \quad (37)$$

where $\lambda_i \in \mathbb{R}^3$ is the vector of the variables in λ corresponding to $\hat{\mathbf{F}}_{\text{int}_i}^B$, $\lambda_{\tau_i} \in \mathbb{R}^2$ is the vector of the variables in λ corresponding to $[\hat{\tau}_{\text{int}_{x_i}} \ \hat{\tau}_{\text{int}_{y_i}}]^T$, A_1 is defined in equation (26), r is the residual computed in equation (23), A_2 along with b_{2i} are defined in equation (32) and b_{3i} is defined from equation (34). The constraints in equation (37) can be expressed the same as in equation (28) by expressing each equality constraint as two inequality constraints (i.e. $a = b$

is equivalent to $a \geq b$, $a \leq b$) and changing the direction of all inequality constraints from \geq to \leq (i.e. $a \geq b$ is equivalent to $-a \leq -b$).

In our experimental setup the problem defined in equation (36) is solved at every time step through the quadratic solver included in the computational geometry algorithms library (CGAL).³

6. Control

In this section, we design a control scheme to drive the UAV based on the external force and torques. The main goal of the control framework is to admit the estimated interaction wrench $\hat{\Lambda}_{\text{int}}$ while rejecting the disturbance wrench $\hat{\Lambda}_{\text{dis}}$. Therefore, these two components will be treated differently inside the controller, which can be divided into two main parts:

- (a) the high level admittance control scheme that uses $\hat{\Lambda}_{\text{int}}$ to compute a reference trajectory;
- (b) the low level trajectory tracking which is in charge of rejecting $\hat{\Lambda}_{\text{dis}}$.

6.1. Admittance control

In the admittance control framework the desired trajectory $\mathbf{p}_d(t), \dot{\mathbf{p}}_d(t), \ddot{\mathbf{p}}_d(t)$ in \mathcal{F}_W is modified based on the estimated interaction forces $\hat{\mathbf{F}}_{\text{int}_i}^B, i = 1, \dots, N$ to provide a reference trajectory for the low level controller $\mathbf{p}_a(t), \dot{\mathbf{p}}_a(t), \ddot{\mathbf{p}}_a(t)$. Let the admittance force \mathbf{F}_a expressed in \mathcal{F}_W be defined as the low-pass filtered resultant of all the $\hat{\mathbf{F}}_{\text{int}_i}$

$$\mathbf{F}_a = \text{low pass} \left(\hat{\mathbf{F}}_{\text{int}}^W \right) = \text{low pass} \left(\sum_{i=1}^n \mathbf{R}_B^W \hat{\mathbf{F}}_{\text{int}_i}^B \right). \quad (38)$$

In theory, the most faithful behavior would be to use directly $\hat{\mathbf{F}}_{\text{int}}^W$. However, $\hat{\mathbf{F}}_{\text{int}}^W$ is a discontinuous signal because it depends on the discretized signal coming from the contact sensors. Therefore, it would cause discontinuous accelerations and commanded attitudes, which are not suitable for safe PHUI. Hence, the role of the low-pass filter is to smooth these discontinuities. Here, a second-order low pass filter with filter time constant $t_f = 0.35$ s is used. The average time step of the estimator is around $t_{\text{step}} = 8$ ms.

In order to modify the desired trajectory, we consider the UAV as an ideal mass-spring-damper system driven by the state equation

$$\ddot{\mathbf{p}}_a = \frac{\mathbf{F}_a + \Delta(\dot{\mathbf{p}}_d - \dot{\mathbf{p}}_a) + \Sigma(\mathbf{p}_d - \mathbf{p}_a) + \mu \ddot{\mathbf{p}}_d}{\mu}, \quad (39)$$

where $\mu \in \mathbb{R}^+$ is the virtual mass, the diagonal positive semidefinite constant matrices $\Delta, \Sigma \in \mathbb{R}^{3 \times 3}$ that define a Hurwitz polynomial are the damping and stiffness constants that are used to change the dynamical response of the UAV. Note that the elements of Δ and Σ are ≥ 0 . The values μ, Δ and Σ can be chosen in order to provide a human

friendly behavior avoiding sudden accelerations and allowing to exert forces on the UAV. In general, their value can be selected independently on each axis. However, in our case we have chosen

$$\Delta = \delta I_3, \quad \Sigma = \sigma I_3, \quad (40)$$

with $\delta = 1, \sigma = 0$ during human friendly interaction in Section 9.1 or varying values of σ as mentioned in Section 9.2 for the trajectory tracking. In order to have a complete reference trajectory in the form $\mathbf{p}_a(t), \dot{\mathbf{p}}_a(t), \ddot{\mathbf{p}}_a(t)$, the values of $\dot{\mathbf{p}}_a$ and \mathbf{p}_a are computed by integrating $\ddot{\mathbf{p}}_a$ in time.

6.2. Trajectory tracking control with wrench feedforward

In order to command the UAV to follow the reference trajectory, we use a control law based on the one proposed by Lee et al. (2010) and improved by Spica et al. (2013) because of its global convergence, aggressive maneuvers capability and excellent trajectory tracking performance. In addition, the controller for the rotational dynamics is developed directly on $SO(3)$ and thereby it avoids any singularities that arise in local coordinates, such as Euler angles. In order to reject the estimated disturbance wrench, we include a feedforward disturbance compensation term.

Considering the trajectory tracking task, at a given time step the tracking error in position and velocity are defined as $\mathbf{e}_p = \mathbf{p}_W - \mathbf{p}_a$ and $\mathbf{e}_v = \dot{\mathbf{p}}_W - \dot{\mathbf{p}}_a$ respectively. The desired force for the translational dynamics is given as

$$\rho = (m\ddot{\mathbf{p}}_a - \mathbf{K}_d \mathbf{e}_v - \mathbf{K}_p \mathbf{e}_p - \mathbf{K}_i \int_{t_0}^t \mathbf{e}_p dt - mge_3 - \hat{\mathbf{F}}_{\text{dis}}) \cdot \mathbf{R}_B^W e_3, \quad (41)$$

where the diagonal positive definite gain matrices $\mathbf{K}_d, \mathbf{K}_p$ and \mathbf{K}_i define Hurwitz polynomials. The desired hovering thrust is realized by $f_z = \rho e_3$ and by aligning the body vertical axis along the direction of the ρ defined as

$$\vec{z}_{R_d} = \frac{m\ddot{\mathbf{p}}_a - \mathbf{K}_d \mathbf{e}_v - \mathbf{K}_p \mathbf{e}_p - \mathbf{K}_i \int_{t_0}^t \mathbf{e}_p dt - mge_3 - \hat{\mathbf{F}}_{\text{dis}}}{\|m\ddot{\mathbf{p}}_a - \mathbf{K}_d \mathbf{e}_v - \mathbf{K}_p \mathbf{e}_p - \mathbf{K}_i \int_{t_0}^t \mathbf{e}_p dt - mge_3 - \hat{\mathbf{F}}_{\text{dis}}\|}, \quad (42)$$

where \vec{z}_{R_d} is the third column of the desired attitude rotation matrix $\mathbf{R}_{B_d}^W$ defined as $\mathbf{R}_{B_d}^W = [\vec{x}_{R_d}, \vec{y}_{R_d}, \vec{z}_{R_d}] \in SO(3)$. Since the quadrotor UAV is an underactuated system, the desired attitude generated by the outer-loop translational dynamics is controlled by the inner-loop torques, that are generated to control the rotational dynamics, to track a desired attitude rotation $\mathbf{R}_{B_d}^W$. The other two columns \vec{x}_{R_d} and \vec{y}_{R_d} of $\mathbf{R}_{B_d}^W$, which account for the remaining degrees of freedom, should be chosen such that their direction is orthogonal to \vec{z}_{R_d} and minimize the yaw error. Therefore

$$\vec{x}_{R_d} = \vec{y}_{R_d} \times \vec{z}_{R_d}, \quad \vec{y}_{R_d} = \frac{\vec{z}_{R_d} \times \vec{x}_{R_d}}{\|\vec{z}_{R_d} \times \vec{x}_{R_d}\|}. \quad (43)$$

For the rotational dynamics, assuming that $\omega_{B_d} = [\mathbf{R}_{B_d}^W \dot{\mathbf{R}}_{B_d}^{W_T}]_\vee$, where $[\cdot]_\vee$ represents the inverse (vee) operator from $so(3) \rightarrow \mathbb{R}^3$, the attitude tracking error $\mathbf{e}_R \in \mathbb{R}^3$ is defined similarly to Lee et al. (2010) as

$$\mathbf{e}_R = \frac{1}{2} [\mathbf{R}_{B_d}^{W_T} \mathbf{R}_B^W - \mathbf{R}_B^{W_T} \mathbf{R}_{B_d}^W]_\vee \quad (44)$$

and the tracking error of the angular velocity $\mathbf{e}_\omega \in \mathbb{R}^3$ is given by

$$\mathbf{e}_\omega = \omega_B - \mathbf{R}_B^{W_T} \mathbf{R}_{B_d}^W \omega_{B_d}. \quad (45)$$

In order to obtain an asymptotic convergence to $\mathbf{0}$ of the rotational error \mathbf{e}_R one can choose the following controller

$$\begin{aligned} \tau = & -\mathbf{K}_\omega \mathbf{e}_\omega - \mathbf{K}_r \mathbf{e}_R - \mathbf{K}_{ir} \int_{t_0}^t \mathbf{e}_R + \omega_B \times \mathbf{I}_B \omega_B - \\ & - \mathbf{I}_B ([\omega_B]_\wedge \mathbf{R}_B^{W_T} \mathbf{R}_{B_d}^W \omega_{B_d} - \mathbf{R}_B^{W_T} \mathbf{R}_{B_d}^W \dot{\omega}_{B_d}) - \hat{\tau}_{dis}, \end{aligned} \quad (46)$$

where the diagonal positive-definite gain matrices \mathbf{K}_ω , \mathbf{K}_r and \mathbf{K}_{ir} define Hurwitz polynomials, $[\omega_B]_\wedge$ is the skew symmetric matrix of ω_B and $\hat{\tau}_{dis}$ is the external torque disturbance.

7. Hardware-in-the-loop physical simulations

In order to verify the wrench estimators and the admittance controller, it is necessary to test the proposed algorithms with the ground truth on the forces and torques applied on the UAV. Recently, it is becoming a trend to perform Hardware-in-the-loop (HIL) simulations to verify various algorithms before their testing on real robot (Cai et al., 2008; Chandrasekaran and Choi, 2010; Odelga et al., 2015).

In our case, the advantage of performing HIL simulations are:

- (a) the hardware and sensors, the software setup and the communication link with the UAV can be tested as in real experiments;
- (b) the wrench estimators can be verified with ground truth data;
- (c) the functionality of the admittance control and the disturbance compensator can be verified without exposing people to any danger;
- (d) the computational times and the feasibility in real-time is tested.

Our HIL simulation setup is based on the one proposed by Odelga et al. (2015) and consists of:

- (a) Gazebo,⁴ a popular open source ROS-enabled simulator, which provides the dynamical simulation of the UAV and feedbacks the corresponding sensor readings (IMU, pose);
- (b) our UAV and contact sensor setup, including the ODROID XU3 board which reads the contact sensor state and communicate it to the base station;

(c) a collection of ROS nodes based on Telekyb software (Grabe et al., 2013) which provide the hardware interfacing, estimation and control functionalities.

Figure 6 shows the block scheme of our HIL simulation setup. The communication between the Odroid board and Gazebo is achieved through ROS topics over IEEE 802.11 connection.

Note that during a HIL simulation the real UAV does not perform any actual flight, being all the flight maneuvers performed only by the simulated UAV. Similarly, the interaction and disturbance forces are applied only virtually to the simulated UAV, but the buttons are pushed on the real sensor ring.

After the takeoff at $t = 8.5$ s the HIL physical simulation is carried out by applying for $t \geq 8.5$ s an external force of $\mathbf{F}_{ext} = [2 \ -2 \ 0]^T$ N in the horizontal frame \mathcal{F}_H on the simulated UAV while it is commanded to stay hovering. Some PoC sensors s_i are pushed at different time instants between $t = 25$ s and $t = 85$ s. Figure 5(a) to (c) reports the external force and the activation states of the sensors. Figure 5(d) to (f) shows the estimated interaction (red) and disturbance (green) forces throughout the whole simulation. Between $t = 8.5$ s and $t = 25$ s, no PoC sensor is active, hence the whole external force is interpreted as a disturbance. The first activated PoC sensors is s_3 , which is active between $t = 25$ s and $t = 30$ s. Since s_3 is oriented along the negative Y -axis, during this time the external force along this direction is interpreted as interaction force. Hence, the interaction force estimated is $\hat{\mathbf{F}}_{int} \approx [0 \ -2 \ 0]^T$ N.

Similarly, interaction forces are estimated as $\hat{\mathbf{F}}_{int} = [2 \ -2 \ 0]^T$ N at $t = 35$ s, $\hat{\mathbf{F}}_{int} = [2 \ 0 \ 0]^T$ N at $t = 45$ s and $\hat{\mathbf{F}}_{int} = [2 \ -2 \ 0]^T$ N at $t = 54$ s through the activation of PoC sensors s_4 and s_5 . At $t = 54$ s, a human interaction is made through multiple contact as can be seen that both s_4 and s_5 are active at the same time in Figures 5(a) to (c). In this case, $\hat{\mathbf{F}}_{int} = \mathbf{J}_{H_4} \hat{\mathbf{F}}_{int_4}^B + \mathbf{J}_{H_5} \hat{\mathbf{F}}_{int_5}^B$.

Between $t = 60$ s and $t = 75$ s we tested the scenario in which the UAV is subject to one or more sudden impacts (i.e. the contact happens only for fractions of seconds) as can be seen through the sensor activation of s_3 in Figsure 5(a) to (c). Figure 5(d) to (f) show that during the contact the disturbance falls to zero and the interaction forces rise from zero, hence the UAV is able to detect these impacts. Clearly, the presence of the low pass filter tends to slow down the rate at which the estimated interaction forces rise, so their absolute value is underestimated. This behavior can be mitigated by differently tuning the low pass filter. However, the time constant of the filter used in this work (provided in Section 6.1) is a good compromise between the need to detect the impacts and the need to provide smooth commanded accelerations and attitude to the UAV.

An interesting case is at $t = 79$ s. A human interaction happens at s_7 , which is in the direction of the positive Y -axis. Although s_7 is active, the external force is $\mathbf{F}_{ext} = [2 \ -2 \ 0]^T$ N, with 2 N force along the negative Y -axis.

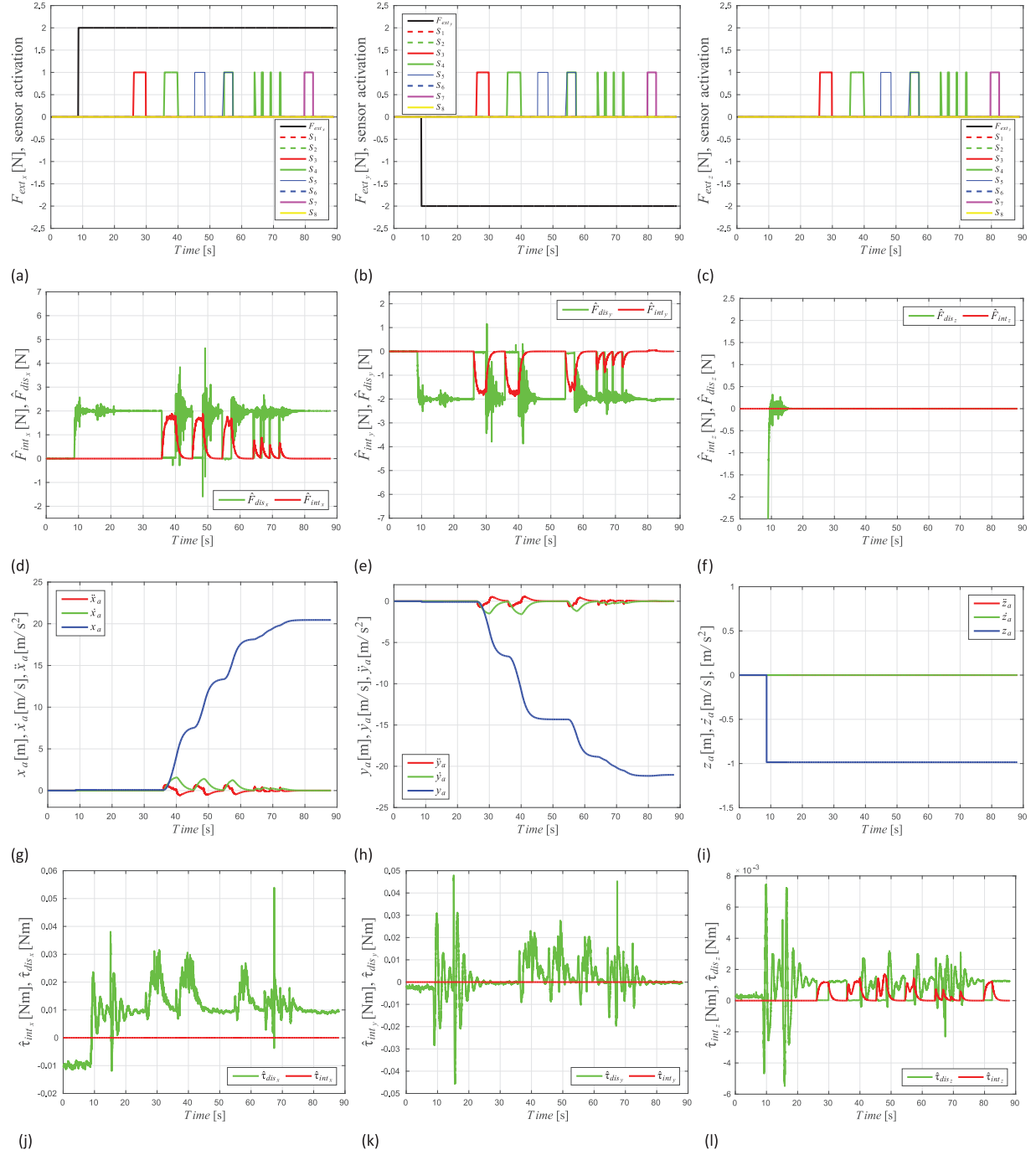


Fig. 5. Results of hardware-in-the-loop simulations. (a) External force applied along the X -axis (black) and sensor ($s_i, \forall i = 1 \rightarrow 8$) activation status for s_1 (dashed red), s_2 (dashed green), s_3 (solid red), s_4 (solid green), s_5 (solid blue), s_6 (dashed blue), s_7 (solid magenta), s_8 (solid yellow). (b) External force applied along the Y -axis (black) and sensor ($s_i, \forall i = 1 \rightarrow 8$) activation status. (c) External force applied along the Z -axis (black) and sensor ($s_i, \forall i = 1 \rightarrow 8$) activation status. (d) Estimated interaction \hat{F}_{int_x} (red) and disturbance \hat{F}_{dis_x} (green) forces along the X -axis. (e) Estimated interaction \hat{F}_{int_y} (red) and disturbance \hat{F}_{dis_y} (green) forces along the Y -axis. (f) Estimated interaction \hat{F}_{int_z} (red) and disturbance \hat{F}_{dis_z} (green) forces along the Z -axis. (g) Admittance acceleration \ddot{x}_a (red), admittance velocity \dot{x}_a (green) and admittance position x_a (blue) along the X -axis. (h) Admittance acceleration \ddot{y}_a (red), admittance velocity \dot{y}_a (green) and admittance position y_a (blue) along the Y -axis. (i) Admittance acceleration \ddot{z}_a (red), admittance velocity \dot{z}_a (green) and admittance position z_a (blue) along the Z -axis. (j) Estimated interaction $\hat{\tau}_{int_x}$ (red) and disturbance $\hat{\tau}_{dis_x}$ (green) torques around the X -axis. (k) Estimated interaction $\hat{\tau}_{int_y}$ (red) and disturbance $\hat{\tau}_{dis_y}$ (green) torques around the Y -axis. (l) Estimated interaction $\hat{\tau}_{int_z}$ (red) and disturbance $\hat{\tau}_{dis_z}$ (green) torques around the Z -axis.

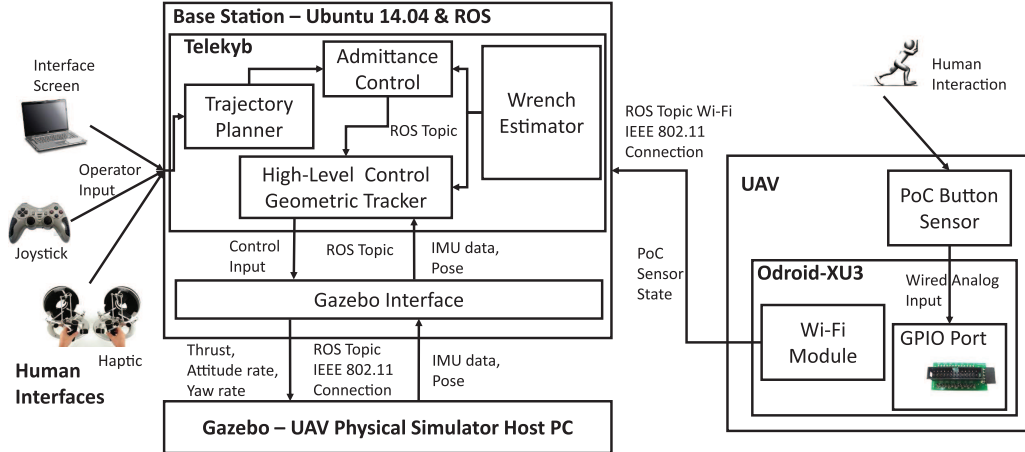


Fig. 6. Block scheme of hardware-in-the-loop setup.

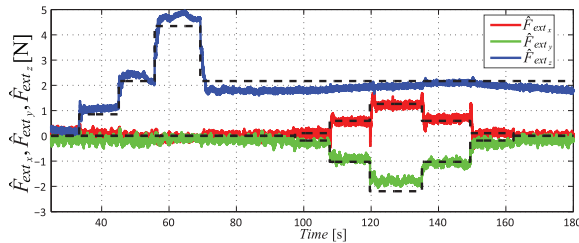


Fig. 7. Results of the experiment with the external force along the X , Y and Z axes. Applied force (black dashed lines), estimated forces \hat{F}_{ext_x} (red), \hat{F}_{ext_y} (green), and \hat{F}_{ext_z} (blue) respectively along the X , Y and Z axes.

This indirectly means that there is no interaction force at s_7 despite being active. Hence, $\hat{\mathbf{F}}_{\text{int}}$ in Figure 5(e) detects a small sensor activation force at $t = 79$ s, whereas all the \mathbf{F}_{ext} is considered as disturbance. This once again proves the effectiveness of the estimator during the separation of human interaction forces from the external disturbances.

Figure 5(g) to (i) show the results of the admittance control where the original desired trajectory (hovering) is modified during the human interaction as a new admittance-based trajectory with acceleration $\ddot{\mathbf{p}}_a$ (red), velocity $\dot{\mathbf{p}}_a$ (green) and position \mathbf{p}_a (blue), expressed in \mathcal{F}_H .

Figures 5(j) to (l) show the estimated disturbance $\hat{\tau}_{\text{dis}}$ (red) and interaction $\hat{\tau}_{\text{int}}$ (green) torques around the three principal axes. Figure 5(j) shows a small constant $\hat{\tau}_{\text{dis}_x}$ of 0.01 Nm estimated around the X -axis which is due to mismatches in the physical parameters of the system. Furthermore, when an interaction force ($\hat{\mathbf{F}}_{\text{int}}$) is applied in the XY plane, it also generates torque disturbances $\hat{\tau}_{\text{dis}_y}$ and $\hat{\tau}_{\text{dis}_z}$ around the X and Y axes (Figure 5(j) to (k)), as predicted by equation (12). Nevertheless, $\hat{\tau}_{\text{int}_x}$ and $\hat{\tau}_{\text{int}_y}$ are always zero due to the constraints in the optimization problem (equation (35)). As the interaction torque around the Z -axis is not constrained, Figure 5(l) shows that very small interaction torques $\hat{\tau}_{\text{int}_z}$ approximately of 0.001 Nm are estimated, once again due to mismatches of the parameters.

Table 1. Root mean square error (RMSE) of the estimated external force $\hat{\mathbf{F}}_{\text{ext}}$ during the first experiment.

Parameter	RMSE	Unit
\hat{F}_{ext_x}	0.1391	N
\hat{F}_{ext_y}	0.2152	N
\hat{F}_{ext_z}	0.3026	N

8. Experimental validation of the external wrench estimator

In a preliminary experimental campaign we have validated the 6D wrench observer (Section 5.1) by subjecting the quadrotor to known external forces and torques while hovering. In order to apply known forces, we have used a weight attached to the CoM of the UAV through a lightweight cable. The known gravity force is applied in different directions (i.e. along the X , Y and Z axes) through the use of a pulley setup. The forces were applied in steps, to test different forces acting on the quadrotor. As shown in Figure 7, at the time instants 32 s, 46 s and 57 s respectively, forces of 0.85 N, 2.17 N and 4.35 N were applied along the Z -axis by adding weights of 87 g, 221 g and 443 g. At time 69 s a weight of 222 g acting along the Z -axis was removed and then at times 97 s, 107 s and 119 s respectively, forces of 0.22 N, 1.19 N and 2.53 N were added along a vector laying on the XY plane and having an azimuth of -60° . To conclude the experiment, these forces were removed in the same order. As shown in Figure 7 the external forces F_{ext_x} (red), F_{ext_y} (green) and F_{ext_z} (blue) were correctly estimated at all time. Table 1 shows the root mean square error (RMSE) of the estimated external force $\hat{\mathbf{F}}_{\text{ext}}$ during this experiment. The low values of the RMSE show the efficiency of this approach.

Two similar experiments were conducted separately to validate the torque estimation. In this case, the ropes connecting the weights to the UAV were not connected to the CoM, but at the end of one arm of the quadrotor to create

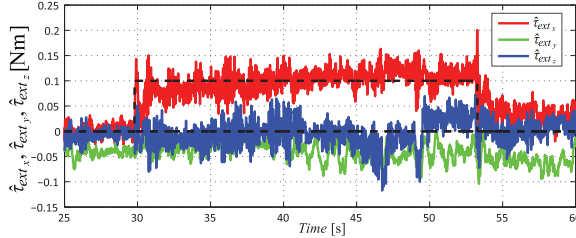


Fig. 8. Results of the experiment with the external torque around the X -axis. Applied torque (black dashed lines), estimated torques $\hat{\tau}_{ext_x}$ (red), $\hat{\tau}_{ext_y}$ (green) and $\hat{\tau}_{ext_z}$ (blue) respectively around the X , Y and Z axes.

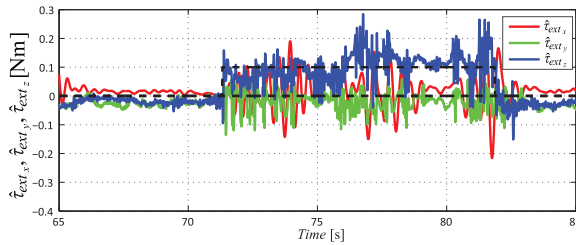


Fig. 9. Results of the experiment with the external torque around the Z -axis. Applied torque (black dashed lines), estimated torques $\hat{\tau}_{ext_x}$ (red), $\hat{\tau}_{ext_y}$ (green) and $\hat{\tau}_{ext_z}$ (blue) respectively around the X , Y and Z axes.

Table 2. Root mean square error (RMSE) of the estimated external torque $\hat{\tau}_{ext}$ during the external torque experiment around the X -axis.

Parameter	RMSE	Unit
$\hat{\tau}_{ext_x}$	0.0270	N m
$\hat{\tau}_{ext_y}$	0.0461	N m
$\hat{\tau}_{ext_z}$	0.0253	N m

known torques. In the first experiment in Figure 8, a weight of 27 g was suspended at a distance of 37.5 cm from the quadrotor CoM along the Y -axis, to generate a torque of 0.099 Nm around the X -axis, which is correctly estimated as τ_{ext_x} (red). A small constant τ_{ext_y} (green) is also estimated during the whole experiment, due to a non perfect balance of the weights on the quadrotor, while τ_{ext_z} (blue) is correctly estimated approximately zero.

In the second torque experiment, a force was applied through our rope-pulleys setup in order to create a torque τ_{ext_z} around the Z -axis. Similarly to the first experiment, a weight of 27 g was suspended at a distance of 37.5 cm from the quadrotor center. As we show in Figure 9, the τ_{ext_z} of 0.099 Nm was correctly estimated (blue). Overall, these experiments prove the effectiveness of the external force/torque estimator. Tables 2 and 3 shows the RMSE of the estimated external torque $\hat{\tau}_{ext}$ during the two external torque experiments.

Table 3. Root mean square error (RMSE) of the estimated external torque $\hat{\tau}_{ext}$ during the external torque experiment around the Z -axis.

Parameter	RMSE	Unit
$\hat{\tau}_{ext_x}$	0.0523	N m
$\hat{\tau}_{ext_y}$	0.0350	N m
$\hat{\tau}_{ext_z}$	0.0415	N m

9. Experimental validation of PHUI

In this section, we present two experiments of human-UAV interaction performed to test our framework. As the main goal of the previous section was to validate the estimator with respect to the ground truth, this section is primarily meant to provide examples of PHUI and show the feasibility of our approach in the real world. In order to check the features of the proposed system, we test it with different interaction modalities (sudden impact, continuous pushing, multiple PoC) and in different situations (hovering, trajectory following).

Therefore, our aim is to show how different behaviors can be obtained using different tuning of the admittance controller, focusing on the stiffness constant σ in equation (40). The other parameters are fixed for all experiments. In particular, the trajectory tracking controller parameters used for the translational dynamics in equation (41) are $\mathbf{K}_d = 5\mathbf{I}_3$, $\mathbf{K}_p = 25\mathbf{I}_3$ and $\mathbf{K}_i = 2\mathbf{I}_3$. Similarly, $\mathbf{K}_\omega = 0.5\mathbf{I}_3$, $\mathbf{K}_r = 1.2\mathbf{I}_3$ and $\mathbf{K}_{ir} = 0.2\mathbf{I}_3$ were used for the rotational dynamics in equation (46). The interested readers are invited to watch the video of the two experiments in the attached Multimedia Extension 1.

9.1. Continuously pushing, sudden impact and multiple PoCs

In the first experiment, the quadrotor is allowed to hover at its take off position while different types of human interaction (continuous pushing, sudden impact and simultaneous multiple contacts) are performed. The plot of the sensor activation is shown in Figure 10(a). Sudden impact contacts are applied for $t \in [25 \text{ s}, 42 \text{ s}]$, $t \in [58 \text{ s}, 68 \text{ s}]$, $t \in [74 \text{ s}, 94 \text{ s}]$ and $t \geq 105 \text{ s}$. In PHUI, sudden impacts may happen either voluntarily (i.e. an operator intentionally pushes away the UAV) or accidentally. In both cases, the UAV should be compliant in order to follow the commands of the operator or to go in the opposite direction with respect to where the contact happens. At $t = 44 \text{ s}$, 52 s and 69 s , continuous interactions are performed at PoC positions s_2 , s_6 and s_4 respectively. Multiple contacts are performed at $t = 99 \text{ s}$ with continuous interaction forces applied both at s_4 and s_6 . These cases are compatible for example with a kinesthetic trajectory learning task, and also in this case the UAV should be completely compliant with the commands of the operator. Therefore, in this experiment we have tuned the admittance controller with stiffness $\sigma = 0$.

Figure 10(c) and (d) show the estimated interaction forces $\hat{\mathbf{F}}_{\text{int}_x}$ and $\hat{\mathbf{F}}_{\text{int}_y}$ respectively. At the end of every human contact, the estimated interaction forces decrease slowly. This desirable behavior is due to the smoothening action of the second-order low-pass filter which reduces the amplitude of the desired acceleration (Figure 10(g) and (h)). Since the translational and rotational dynamics of the quadrotor are coupled (see equations (5) to (7)), reduced desired accelerations means also reduced desired pitch θ_d and roll ϕ_d , and smaller angular rates. Hence, the introduction of the low-pass filter helps the system to keep smooth, human-friendly behavior where no sudden acceleration or rotation is performed.

Figure 10(e) and (f) show the estimated external disturbance $\hat{\mathbf{F}}_{\text{dis}_x}$ and $\hat{\mathbf{F}}_{\text{dis}_y}$ respectively. At the end of every sudden impact, a spike in $\hat{\mathbf{F}}_{\text{dis}}$ is clearly visible. This happens because the dynamics of the UAV are heavily perturbed by a sudden impact, hence strong disturbance terms are estimated during and after the contact. However, a substantial fraction of the external force exerted by the user is still detected as interaction force, enough to detect the impact. As expected, during the continuous pushing scenarios this effect is either not present or negligible. Applying an adaptive law to the weights in the optimization process, and/or introducing a hysteresis mechanism in the button activation process could help to mitigate this effect.

The reference trajectory produced by the admittance controller with the modified acceleration $\dot{\mathbf{p}}_a$ (in red), velocity $\dot{\mathbf{p}}_a$ (in green) and position \mathbf{p}_a (in blue) is shown in Figure 10(g) and (h). The trajectory shows a smooth behavior thanks to the smoothing of the admittance force \mathbf{F}_a performed by the low-pass filtering applied on $\hat{\mathbf{F}}_{\text{int}}$. Figure 10(b) shows the XY plot of the position of the UAV during the experiment.

Figure 10(i) and (j) show the estimated external disturbance torques $\hat{\tau}_{\text{dis}_x}$ and $\hat{\tau}_{\text{dis}_y}$ respectively. While small non-zero mean values are due to a non-perfect balancing of the weights on the UAV, the spikes are caused by the application of the interaction forces which perturb the UAV dynamics, in particular in the case of sudden impacts.

9.2. Trajectory tracking during human interaction with varying stiffness

In this experiment, the quadrotor is given a trajectory tracking task to follow a circle of 3 m diameter (shown in blue in Figure 11(a) to (c)) with a constant linear velocity of 0.3 m/s. Human contact is made at different PoC positions and \mathbf{F}_{int} is applied to change the desired trajectory. Three experiments were performed with different stiffness constant values σ while following the circular trajectory. In general, the value of the stiffness σ decides the behavior of the quadrotor not only during the interaction phase, but also after the end of the interaction.

Initially, the experiment is carried out with the stiffness constant $\sigma = 0$. The XY plot in Figure 11(a) compares the actual (red) and reference (blue) trajectories. The estimated

interaction forces $\hat{\mathbf{F}}_{\text{int}_x}$ and $\hat{\mathbf{F}}_{\text{int}_y}$ are shown in Figure 11(d). The plots show that whenever a force is applied, its value is estimated and the trajectory is changed according to its magnitude. Hence, the original circular reference trajectory is modified to the new translated circular admittance trajectory \mathbf{p}_a which is tracked by the UAV. The estimated $\hat{\mathbf{F}}_{\text{dis}_x}$ and $\hat{\mathbf{F}}_{\text{dis}_y}$ are shown in Figure 11(g). This case is once again compatible with applications in which the UAV must follow the lead of the human. For example, if the UAV has to perform a prefixed trajectory (e.g. for monitoring, inspection, target tracking, data collection, etc.) in a place specified by an untrained operator.

The results of the same trajectory tracking task performed with stiffness $\sigma = 0.1$ are shown in Figure 11(b), (e) and (h). Also in this case the trajectory is modified by the presence of $\hat{\mathbf{F}}_{\text{int}_x}$ and $\hat{\mathbf{F}}_{\text{int}_y}$. However, thanks to the non-zero stiffness in the admittance control, every time the UAV is able to come back to follow the original desired circular trajectory. The convergence speed is nevertheless very slow, and it takes more than one circle for the robot to recover the initial trajectory.

In the third test (Figure 11(c), (f) and (i)), the same circular trajectory tracking task is carried out with $\sigma = 0.5$. Due to the larger stiffness in the admittance control, the controller acts immediately on the position error generating a \mathbf{p}_a which tries to bring the quadrotor back to the original trajectory as fast as possible. Hence, each interacting force leaves only a small bump in the trajectory (Figure 11(c)).

In both cases in which the stiffness is greater than zero, the UAV shows a compliant behavior but also goes back to the original trajectory. Hence, they are compatible with a situation in which the UAV is in charge of delivering one or more objects (e.g. tools) to one or more humans without landing. In fact, in such a situation the UAV should show some compliance in order to facilitate the pick-up operation, but should also come back to the prefixed trajectory in order to continue the task after the pick-up from one of the recipient. The stiffness could be set higher or lower depending on the type and length of the trajectory, the distance between the operators and the type of object that should be picked up. Additional studies can be carried out in order to determine the optimal stiffness to facilitate the pick-up operation.

10. Conclusions and future works

In this work, we have presented a hardware setup for PHUI that offers the possibility to exchange, detect and characterize interaction forces between humans and UAVs. After modeling the external wrench acting on a UAV as the sum of interaction forces and disturbances, we have developed a methodology to separate them based on residual estimation and quadratic programming. The estimated values are used in an admittance control paradigm which modifies the desired trajectory on the basis of the human interaction.

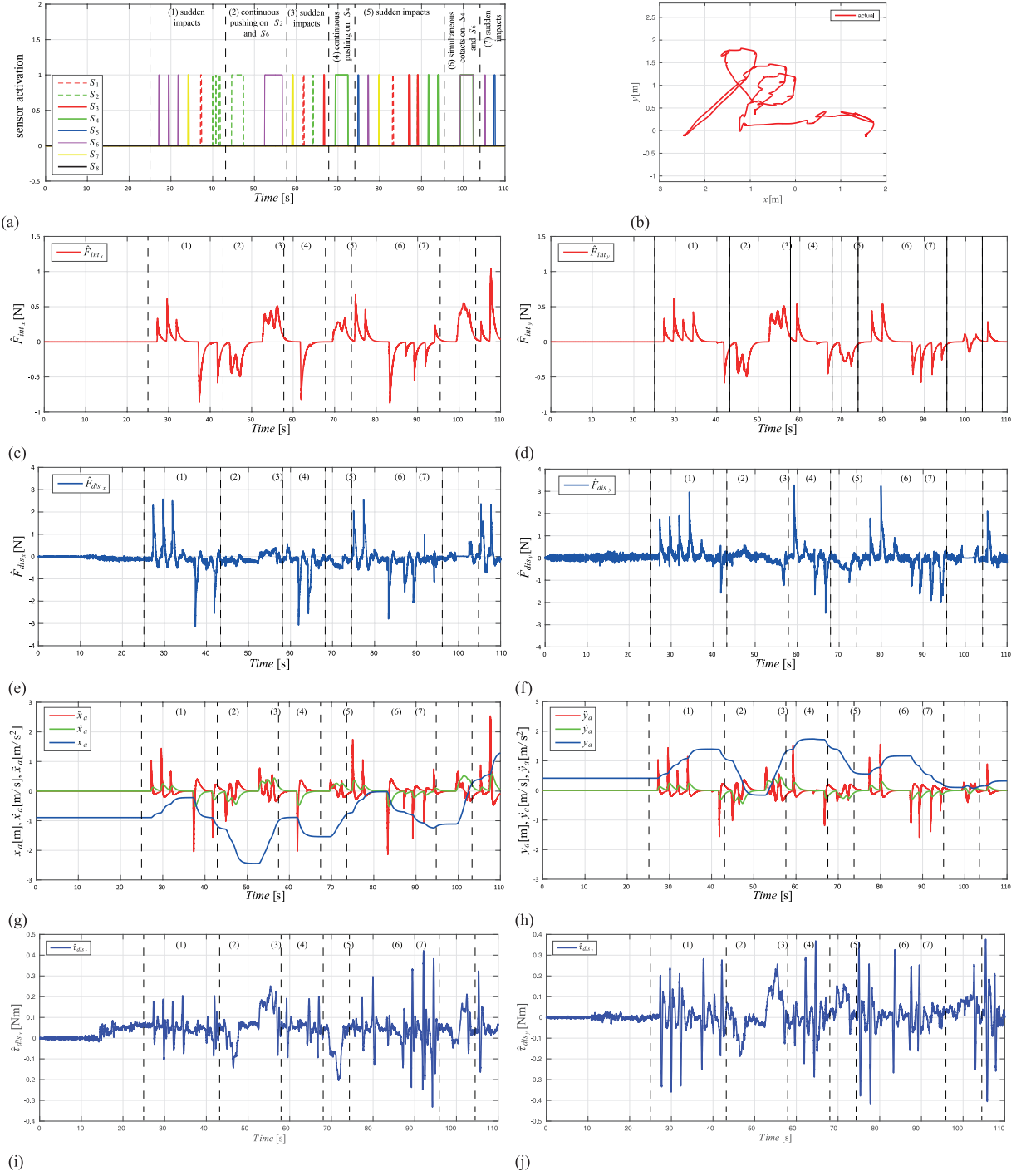


Fig. 10. Results of the continuous pushing, sudden impact and multiple points of contact experiment. (a) Sensor ($s_i, \forall i = 1 \rightarrow 8$) activation status for s_1 (dashed red), s_2 (dashed green), s_3 (solid red), s_4 (solid green), s_5 (solid blue), s_6 (solid magenta), s_7 (solid yellow) and s_8 (solid black). (b) Two dimensional XY plot of the UAV position during the experiment. (c) Estimated interaction force \hat{F}_{int_x} along the X-axis. (d) Estimated interaction force \hat{F}_{int_y} along the Y-axis. (e) Estimated disturbance force \hat{F}_{dis_x} along the X-axis. (f) Estimated disturbance force \hat{F}_{dis_y} along the Y-axis. (g) Admittance acceleration \ddot{x}_a (red), admittance velocity \dot{x}_a (green) and admittance position x_a (blue) along the X-axis. (h) Admittance acceleration \ddot{y}_a (red), admittance velocity \dot{y}_a (green) and admittance position y_a (blue) along the Y-axis. (i) Estimated disturbance torque $\hat{\tau}_{dis_x}$ around the X-axis. (j) Estimated disturbance torque $\hat{\tau}_{dis_y}$ around the Y-axis.

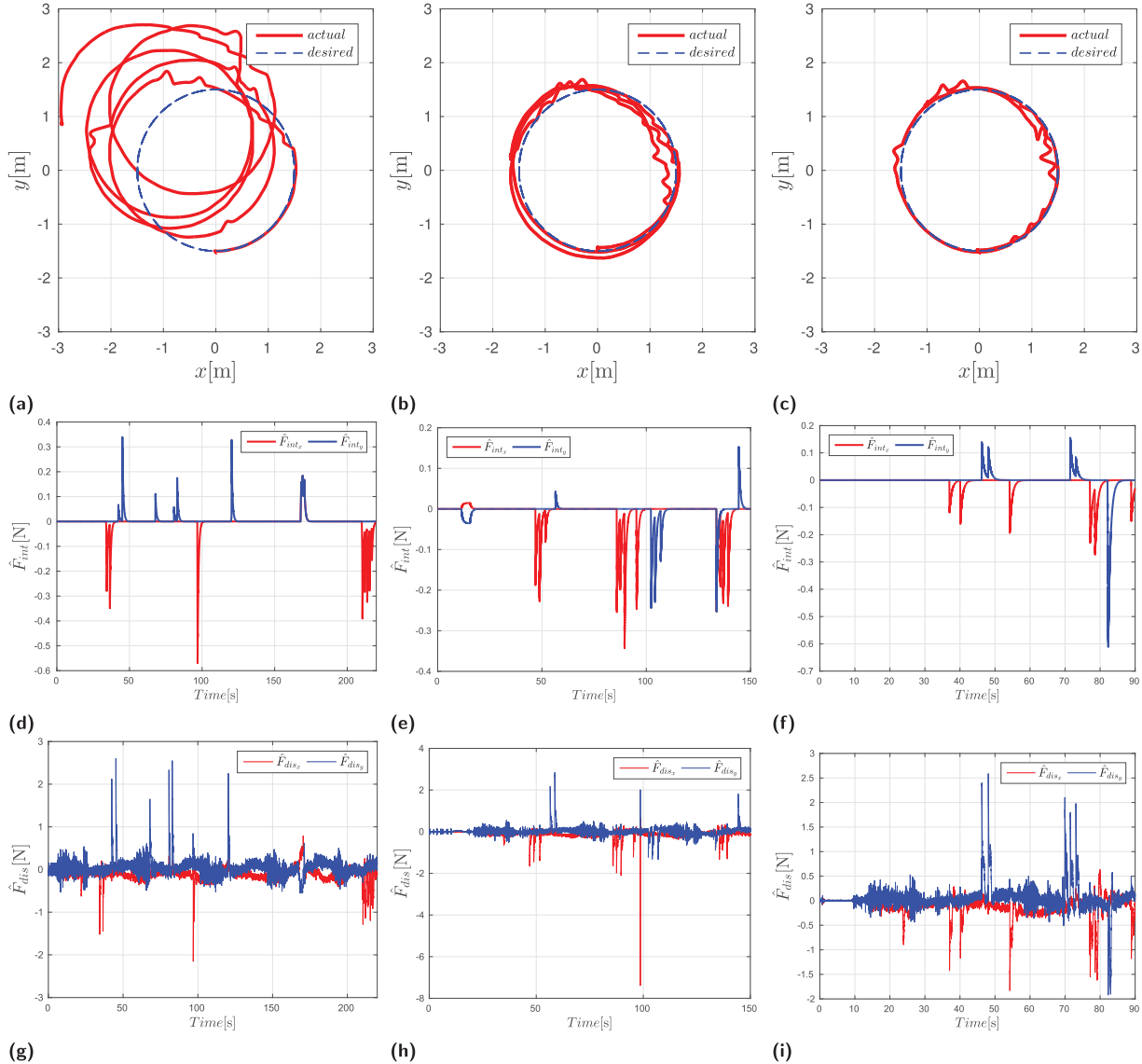


Fig. 11. Results of the trajectory tracking experiment during human interaction with varying stiffness parameter. (a) to (c): Two dimensional XY plot of UAV tracking a circular trajectory during human interaction with stiffness constant 0.0, 0.1 and 0.5, respectively. (d) to (f): Estimated interaction force along X-axis (\hat{F}_{int_x}) and Y-axis (\hat{F}_{int_y}) with stiffness constant 0.0, 0.1 and 0.5 respectively. (g) to (i): Estimated disturbance along the X-axis (\hat{F}_{dis_x}) and Y-axis (\hat{F}_{dis_y}) with stiffness constant 0.0, 0.1 and 0.5, respectively.

The estimated disturbances are instead rejected through a modified geometric tracking controller. We have performed simulations and experiments assuming different scenarios as continuous human contact, sudden impact and multiple points of contact. The results validate the effectiveness of our approach.

Although providing an interaction surface already accounts for some form of safety, in the future we aim to improve our hardware design to offer a larger 3D surface which fully encloses the propellers with full protection for the user, similar to the gimbal (Briod et al., 2014). As byproduct, we also plan to deploy the sensors three-dimensionally and extend our methodology to the case of

a fully actuated UAV, which would allow the human to command also the rotational degrees of freedom.

A shortcoming of the proposed estimation approach is when both interaction and disturbance wrenches occur in the same direction. Further studies could be done to address this limitation, e.g. by developing an adaptive law for the weight in equation (29). Moreover, the current estimation procedure does not provide any quantification of uncertainty or confidence in the wrench estimates, and developing an index of the quality of the estimates based on statistical considerations could be beneficial to reduce noise, outliers and spikes in the behavior of the robot.

The validation proposed in Section 9 includes only experiments in which the user pushes the quadrotor activating the buttons near the point of contact. If instead the quadrotor is pulled, we expect the buttons opposite to the point of contact to be activated, and interaction forces in these locations to be estimated. While we believe that in this scenario our system would work as well (i.e. the UAV would move as if the correct pulling forces were estimated in the real point of contact), and a few preliminary experiments not presented in this work have been successful, a thorough theoretical analysis to study sensor configurations that allow pulling and further experimental results are needed.

Now that the platform is ready for use, we want to employ it in studies with human subjects. In particular, we plan to:

- (a) study the expected interaction behavior by humans;
- (b) further develop and tune the control system of the UAV.

Acknowledgements

The authors would like to thank Jannik Romanowski from the mechanical workshop of the Max Planck Institute for Biological Cybernetics, Tübingen, for his effort in the design and the manufacture of the quadrotor hardware. The authors would also like to thank the anonymous reviewers for their valuable comments and suggestions to improve the quality of the paper.

Funding

The author(s) disclosed receipt of the following financial support for the research, authorship, and/or publication of this article: The work of Sujit Rajappa and Paolo Stegagno was supported by PhD and Research Scientist stipends from the Max Planck Society.

Notes

1. Note that in the work by Lee et al. (2013), the dynamical model in equations (5) to (7) is derived in the North-East-Down frame, while in this paper we present the equivalent model in the North-West-Up frame.
2. <http://www.mikrokopter.de/>
3. <http://www.cgal.org/>
4. <http://gazebosim.org/>

References

- Albers A, Trautmann S, Howard T, et al. (2010) Semi-autonomous flying robot for physical interaction with environment. In: *IEEE conference robotics automation and mechatronics*, Singapore, 28–30 June 2010, pp.441–446. DOI: 10.1109/RAMECH.2010.5513152.
- Alexis K, Nikolakopoulos G and Tzes A (2011) Switching model predictive attitude control for a quadrotor helicopter subject to atmospheric disturbances. *Control Engineering Practice* 19(10): 1195–1207.
- Antonelli G, Arrichiello F, Chiaverini, et al. (2013) Adaptive trajectory tracking for quadrotor MAVs in presence of parameter uncertainties and external disturbances. In: *IEEE/ASME international conference on advanced intelligent mechatronics*, Wollongong, NSW, Australia, 9–12 July 2013, pp.1337–1342. DOI: 10.1109/AIM.2013.6584280.
- Augugliaro F and D'Andrea R (2013) Admittance control for physical human-quadcopter interaction. In: *European control conference*, 2013, pp.1805–1810.
- Augugliaro F, Lupashin S, Hamer M, et al. (2014) The flight assembled architecture installation: Cooperative construction with flying machines. *IEEE Control Systems Magazine* 34(4): 46–64.
- Bellens S, De Schutter J and Bruyninckx H (2012) A hybrid pose/wrench control framework for quadrotor helicopters. In: *IEEE international conference on robotics and automation*, Saint Paul, MN, USA, 14–18 May 2012, pp.2269–2274. DOI: 10.1109/ICRA.2012.6224682.
- Bouabdallah B and Siegwart R (2005) Backstepping and sliding-mode techniques applied to an indoor micro quadrotor. In: *IEEE international conference on robotics and automation*, Barcelona, Spain, 18–22 April 2005, pp.47–52. DOI: 10.1109/ROBOT.2005.1570447.
- Bouabdallah S and Siegwart R (2007) Full control of a quadrotor. In: *IEEE international conference on intelligent robots and systems*, San Diego, CA, USA, 29 October–2 November 2007, pp.153–158. DOI: 10.1109/IROS.2007.4399042.
- Briod A, Kornatowski P, Zufferey JC, et al. (2014) A collision-resilient flying robot. *Journal of Field Robotics* 31(4): 496–509.
- Cai G, Chen B, Lee T, et al. (2008) Design and implementation of a hardware-in-the-loop simulation system for small-scale UAV helicopters. In: *IEEE international conference on automation and logistics*, Qingdao, China, 1–3 September 2008, pp.29–34. DOI: 10.1109/ICAL.2008.4636114.
- Cauchard J, Jane E, Zhai K, et al. (2015) Drone and me: An exploration into natural human-drone interaction. In: *Proceedings of the 2015 ACM international joint conference on pervasive and ubiquitous computing*, Osaka, Japan, 7–11 September 2015, pp.361–365. DOI: 10.1145/2750858.2805823.
- Cauchard J, Zhai K, Spadafora M, et al. (2016) Emotion encoding in human-drone interaction. In: *2016 11th ACM/IEEE international conference on human-robot interaction (HRI)*, Christchurch, New Zealand, 7–10 March 2016, pp.263–270.
- Chandrasekaran K and Choi E (2010) Fault tolerance system for UAV using hardware in the loop simulation. In: *International conference on new trends in information science and service science (NISS)*, Gyeongju, South Korea, 11–13 May 2010, pp.293–300.
- De Luca A and Mattone R (2003) Actuator failure detection and isolation using generalized momenta. In: *IEEE international conference on robotics and automation*, Taipei, Taiwan, 14–19 September 2003, pp.634–639. DOI: 10.1109/ROBOT.2003.1241665.
- Derafa L, Benallegue A and Fridman L (2012) Super twisting control algorithm for the attitude tracking of a four rotors UAV. *Journal of the Franklin Institute* 349(2): 685–699.
- Edsinger A and Kemp CC (2007) Human-robot interaction for cooperative manipulation: Handing objects to one another. In: *16th IEEE international symposium on robot and human interactive communication*, Jeju, South Korea, 26–29 August 2007, pp.1167–1172. DOI: 10.1109/ROMAN.2007.4415256.
- Fraundorfer F, Heng L, Honegger D, et al. (2012) Vision-based autonomous mapping and exploration using a quadrotor

- MAV. In: *IEEE international conference on intelligent robots and systems*, Vilamoura, Portugal, 7–12 October 2012. DOI: 10.1109/IROS.2012.6385934.
- Fumagalli M and Carloni R (2013) A modified impedance control for physical interaction of UAVs. In: *IEEE international conference on intelligent robots and systems*, Tokyo, Japan, 3–7 November 2013, pp.1979–1984. DOI: 10.1109/IROS.2013.6696619.
- Fumagalli M, Naldi R, Macchelli A, et al. (2012) Modeling and control of a flying robot for contact inspection. In: *IEEE international conference on intelligent robots and systems*, Vilamoura, Portugal, 7–12 October 2012, pp.3532–3537. DOI: 10.1109/IROS.2012.6385917.
- Gioioso G, Ryll M, Prattichizzo D, et al. (2014) Turning a near-hovering controlled quadrotor into a 3D force effector. In: *IEEE international conference on robotics and automation*, Hong Kong, China, 31 May–7 June 2014, pp.6278–6284. DOI: 10.1109/ICRA.2014.6907785.
- Grabe V, Riedel M, Bülthoff H, et al. (2013) The TeleKyb framework for a modular and extendable ROS-based quadrotor control. In: *European conference on mobile robots*, Barcelona, Spain, 25–27 September 2013, pp.19–25. DOI: 10.1109/ECMR.2013.6698814.
- Kronander K and Billard A (2014) Learning compliant manipulation through kinesthetic and tactile human-robot interaction. *IEEE Transactions on Haptics* 7(3): 367–380.
- Heng L, Meier L, Tanskanen P, et al. (2011) Autonomous obstacle avoidance and maneuvering on a vision-guided MAV using on-board processing. In: *IEEE international conference on robotics and automation*, Shanghai, China, 9–13 May 2011. DOI: 10.1109/ICRA.2011.5980095.
- Lee D, Franchi A, Son H, et al. (2013) Semiautonomous haptic teleoperation control architecture of multiple unmanned aerial vehicles. *IEEE/ASME Transactions on Mechatronics* 18(4): 1334–1345.
- Lee T, Leok M and McClamroch H (2010) Geometric tracking control of a quadrotor UAV on SE(3). In: *IEEE conference on decision and control*, Atlanta, GA, USA, 15–17 December 2010, pp.5420–5425. DOI: 10.1109/CDC.2010.5717652.
- Lichtenstern M, Frassl M, Perun B, et al. (2012) A prototyping environment for interaction between a human and a robotic multi-agent system. In: *2012 ACM/IEEE international conference on human-robot interaction*, Boston, USA, 5–8 March 2012, pp.185–186. DOI: 10.1145/2157689.2157747.
- Lindsey Q, Mellinger D and Kumar V (2011) Construction of cubic structures with quadrotor teams. In: *Robotics: Science and systems*, Los Angeles, USA, 27–30 June 2011 DOI: 10.15607/RSS.2011.VII.025.
- Lippiello V and Ruggiero F (2012) Exploiting redundancy in Cartesian impedance control of UAVs equipped with a robotic arm. In: *IEEE international conference on intelligent robots and systems*, Vilamoura, Portugal, 7–12 October 2012, pp.3768–3773. DOI: 10.1109/IROS.2012.6386021.
- Lupashin S, Schöllig A, Sherback M, et al. (2010) A simple learning strategy for high-speed quadrocopter multi-flips. In: *IEEE international conference on robotics and automation*, Alaska, USA, 3–7 May 2010 pp.1642–1648. DOI: 10.1109/ROBOT.2010.5509452.
- Magrini E, Flacco F and De Luca A (2014) Estimation of contact forces using a virtual force sensor. In: *IEEE international conference on intelligent robots and systems*, Chicago, IL, USA, 14–18 September 2014, pp.2126–2133. DOI: 10.1109/IROS.2014.6942848.
- Mellinger D, Michael N and Kumar V (2012) Trajectory generation and control for precise aggressive maneuvers with quadrotors. *The International Journal of Robotics Research* 31(5): 664–674.
- Monajjemi V, Wawerla J, Vaughan R, et al. (2013) HRI in the sky: Creating and commanding teams of UAVs with a vision-mediated gestural interface. In: *2013 IEEE/RSJ international conference on intelligent robots and systems*, Tokyo, Japan, 3–7 November 2013, pp.617–623. DOI: 10.1109/IROS.2013.6696415.
- Mueggler E, Faessler M, Fontana F, et al. (2014) Aerial-guided navigation of a ground robot among movable obstacles. In: *IEEE international symposium on safety, security, and rescue robotics (SSRR)*, Hokkaido, Japan, 27–30 October 2014. DOI: 10.1109/SSRR.2014.7017662.
- Nagi J, Giusti A, Caro GAD, et al. (2014) Human control of UAVs using face pose estimates and hand gestures. In: *2014 ACM/IEEE international conference on human-robot interaction*, Bielefeld, Germany, 3–6 March 2014, pp.252–253. DOI: 10.1145/2559636.2559833.
- Naseer T, Sturm J and Cremers D (2013) FollowMe: Person following and gesture recognition with a quadrocopter. In: *2013 IEEE/RSJ international conference on intelligent robots and systems*, Tokyo, Japan, 3–7 November 2013, pp.624–630. DOI: 10.1109/IROS.2013.6696416.
- Ng WS and Sharlin E (2011) Collocated interaction with flying robots. In: *IEEE international symposium on robot and human interactive communication*, Atlanta, USA, 31 July–3 August 2011, pp.143–149. DOI: 10.1109/ROMAN.2011.6005280.
- Nguyen H and Lee D (2013) Hybrid force/motion control and internal dynamics of quadrotors for tool operation. In: *IEEE international conference on intelligent robots and systems*, Tokyo, Japan, 3–7 November 2013, pp.3458–3464. DOI: 10.1109/IROS.2013.6696849.
- Odelga M, Stegagno P, Bülthoff H, et al. (2015) A setup for multi-UAV hardware-in-the-loop simulations. In: *3rd IFAC workshop on research, education and development of unmanned aerial systems*, Cancun, Mexico, 23–25 November 2015. DOI: 10.1109/RED-UAS.2015.7441008.
- Orsag M, Korpela C and Oh P (2013) Modeling and control of MM-UAV: Mobile manipulating unmanned aerial vehicle. *Journal of Intelligent and Robotic Systems* 69(1–4): 227–240.
- Palunko I, Cruz P and Fierro R (2012) Agile load transportation: Safe and efficient load manipulation with aerial robots. *IEEE Robotics and Automation Magazine* 19(3): 69–79.
- Pfeil K, Seng Lee K and LaViola J (2013) Exploring 3D gesture metaphors for interaction with unmanned aerial vehicles. In: *2013 International conference on intelligent user interfaces*, Santa Monica, USA, 19–22 March 2013, pp.257–266. DOI: 10.1145/2449396.2449429.
- Pounds P, Bersak D and Dollar A (2011) Grasping from the air: Hovering capture and load stability. In: *IEEE international conference on robotics and automation*, Shanghai, China, 9–13 May 2011, pp.2491–2498. DOI: 10.1109/ICRA.2011.5980314.
- Quigley M, Goodrich M and Beard R (2004) Semi-autonomous human-UAV interfaces for fixed-wing mini-UAVs. In: *IEEE/RSJ international conference on intelligent robots and systems (IROS)*, Sendai, Japan, 28 September–2 October 2004, vol.3, pp.2457–2462. DOI: 10.1109/IROS.2004.1389777.

- Raffo G, Ortega M and Rubio F (2010) An integral predictive/nonlinear H_∞ control structure for a quadrotor helicopter. *Control Engineering Practice* 46(1): 29–39.
- Rajappa S, Masone C, Bülthoff H, et al. (2016) Adaptive super twisting controller for a quadrotor UAV. In: *IEEE international conference on robotics and automation*, Stockholm, Sweden, 16–21 May 2016, pp.2971–2977. DOI: 10.1109/ICRA.2016.7487462.
- Rajappa S, Ryll M, Bülthoff H, et al. (2015) Modeling, control and design optimization for a fully-actuated hexarotor aerial vehicle with tilted propellers. In: *IEEE international conference on robotics and automation*, Seattle, USA, 26–30 May 2015, pp.4006–4013. DOI: 10.1109/ICRA.2015.7139759.
- Ritz R, Müller M, Hehn M, et al. (2012) Cooperative quadrocopter ball throwing and catching. In: *IEEE international conference on intelligent robots and systems*, Vilamoura, Portugal, 7–12 October 2012, pp.4972–4978. DOI: 10.1109/IROS.2012.6385963.
- Roberts A and Tayebi A (2009) Adaptive position tracking of VTOL UAVs. In: *IEEE conference on decision and control*, Shanghai, China, 15–18 December 2009, pp.5233–5238. DOI: 10.1109/CDC.2009.5400947.
- Ruggiero F, Cacace J, Sadeghian H, et al. (2014) Impedance control of VToL UAVs with a momentum-based external generalized forces estimator. In: *IEEE international conference on robotics and automation*, Hong Kong, China, 31 May–7 June 2014, pp.2093–2099. DOI: 10.1109/ICRA.2014.6907146.
- Sanna A, Lamberti F, Paravati G, et al. (2013) A Kinect-based natural interface for quadrotor control. *Entertainment Computing* 4(3): 179–186.
- Scholten J, Fumagalli M, Stramigioli S, et al. (2013) Interaction control of an UAV endowed with a manipulator. In: *IEEE international conference on robotics and automation*, Karlsruhe, Germany, 6–10 May 2013, pp.4910–4915. DOI: 10.1109/ICRA.2013.6631278.
- Sharma M, Hildebrandt D, Newman G, et al. (2013) Communicating affect via flight path: Exploring use of the Laban effort system for designing affective locomotion paths. In: *8th ACM/IEEE international conference on human-robot interaction*, Tokyo, Japan, 3–6 March 2013, pp.293–300. DOI: 10.1109/HRI.2013.6483602.
- Spica R, Giordano P, Ryll M, et al. (2013) An open-source hardware/software architecture for quadrotor UAVs. In: *2nd IFAC workshop on research, education and development of unmanned aerial systems*, Compiègne, France, 20–22 November 2013. DOI: 10.3182/20131120-3-FR-4045.00006.
- Szafir D, Mutlu B, and Fong T (2015) Communicating directionality in flying robots. In: *10th Annual ACM/IEEE international conference on human-robot interaction*, Portland, USA, 2–5 March 2015, pp.19–26. DOI: 10.1145/2696454.2696475.
- Takakura S, Murakami T and Ohnishi K (1989) An approach to collision detection and recovery motion in industrial robot. In: *IEEE 15th annual conference of industrial electronics society*, Philadelphia, PA, USA, 6–10 November 1989, pp.421–426. DOI: 10.1109/IECON.1989.69669.
- Tomic T and Haddadin S (2015) Simultaneous estimation of aerodynamic and contact forces in flying robots: Applications to metric wind estimation and collision detection. In: *IEEE international conference on robotics and automation*, Seattle, WA, USA, 26–30 May 2015, pp.5290–5296. DOI: 10.1109/ICRA.2015.7139937.
- Yüksel B, Secchi C, Bülthoff H, et al. (2014) A nonlinear force observer for quadrotors and application to physical interactive tasks. In: *IEEE/ASME international conference on advanced intelligent mechatronics*, Besançon, France, 8–11 July 2014, pp.433–440. DOI: 10.1109/AIM.2014.6878116.

Appendix

Index to multimedia extension

Extension	Media type	Description
1	Video	Two experiments of human-UAV interaction